Int J Earth Sci (Geol Rundsch) (2006) 95: 629–647
DOI 10.1007/s00531-005-0060-8

ORIGINAL PAPER

Hilke Timmermann · Wolfgang Dörr · Erwin Krenn
Fritz Finger · Gernold Zulauf

Conventional and in situ geochronology of the Teplá Crystalline unit, Bohemian Massif: implications for the processes involving monazite formation

Received: 18 October 2004 / Accepted: 22 October 2005 / Published online: 22 December 2005

Abstract The Teplá Crystalline unit (TCU), western Bohemian Massif, proves highly suitable for studying the effects of differential metamorphic reworking on the U–Th–Pb systematics in monazite, as the overprint of Variscan regional metamorphism onto high-grade Cadomian paragneisses intensifies progressively towards the northwest. Although variably hampered by scarcity, small size, and low uranium contents of monazite, isotope dilution–thermal ionisation mass spectrometry of monazite from paragneisses from the garnet, staurolite, and kyanite zones of the TCU gives a narrow $^{206}Pb/^{238}U$ age range from 387 to 382 Ma for Variscan peak metamorphism. These data are supported by 382–373 Ma monazite ages derived from electron microprobe analyses. Inheritance of older components in grains from the central TCU imply major "resetting" of pre-Variscan monazite around 380 Ma, possibly due to widespread garnet growth during Variscan metamorphism, which led to the consumption of pre-Variscan high-Y monazite and subsequent growth of new low-Y monazite. Concordant 498–494 Ma monazite ages in a migmatitic paragneiss close to the adjacent Mariánské Lázně Complex (MLC) grew in response to metagabbro emplacement in the MLC from 503 to 496 Ma and not during either Cadomian or Variscan regional metamorphism. Backscatter imaging and electron microprobe analyses reveal that discordant monazite of the migmatite comprises a mix of various age domains that range from ca. 540 to 380 Ma. Combined evidence presented here suggests that instead of Pb loss by volume diffusion, the apparent resetting of the U–Th–Pb systematics in monazite rather involves new crystal growth or regrowth by recrystallisation and dissolution/reprecipitation.

Keywords U–Pb geochronology electron microprobe analysis · Monazite · Teplá Crystalline unit · Bohemian Massif

H. Timmermann (✉) · W. Dörr
Institut für Geowissenschaften, Justus-Liebig Universität,
Senckenbergstr. 3, 35390 Giessen, Germany
E-mail: hilke.timmermann@online.de
Tel.: +49-641-9936016
Fax: +49-641-9936019

E. Krenn · F. Finger
Institut für Mineralogie, Universität Salzburg,
Hellbrunner Str. 34, 5020 Salzburg, Germany

G. Zulauf
Institut für Geologie und Mineralogie,
Universität Erlangen-Nürnberg, Schlossgarten 5,
91054 Erlangen, Germany

Introduction

U–Pb geochronology of monazite has become a widely applied technique for constraining the thermal history of high-grade terranes. Monazite is a light rare earth element (LREE) phosphate that grows in a wide variety of metamorphic and magmatic rocks, including metasediments of amphibolite facies and granulite facies grade, peraluminous (S-type) granites, and rocks interacting with hydrothermal fluids. Major advantages for using monazite are the high contents of uranium and thorium, and thus of accumulated radiogenic Pb, whereas the amount of common Pb—initial Pb incorporated into the crystal structure during crystallisation of the mineral—is generally very low. Furthermore, the high closure temperature (T_c; Dodson 1973) of 700–750°C (e.g. Copeland et al. 1988; Parrish 1990; Heaman and Parrish 1991; Suzuki et al. 1994; Smith and Giletti 1997) with respect to diffusional loss of radiogenic Pb—some authors even suggest T_c in excess of 750–850°C (Spear and Parrish 1996; Rubatto et al. 2001; Cherniak et al. 2004)—implies that monazite is very resistant against thermally driven resetting. Recent studies, however, show that monazite from complexly metamorphosed areas may record many of the stages of its evolution, such as inheritance, Pb loss, or recrystallisation, resulting in either discordant ages or a completely reset U–Pb systematic (e.g. Zhu et al.

1997; Vavra and Schaltegger 1999; Foster et al. 2002). Classic monazite studies assumed parameters such as temperature and grain size (i.e. diffusion as the main process), and crystal plastic deformation to have the most significant impact on the U–Th–Pb system of monazite (e.g. Parrish 1990; Suzuki et al. 1994). More recently, the presence of hot metamorphic fluids has been invoked to dissolve and reprecipitate monazite (e.g. De Wolf et al. 1993; Crowley and Ghent 1999; Townsend et al. 2000; Finger et al. 2002). These factors, controlling the stability of the U–Th–Pb system, must be accurately constrained in order to be able to rightly interpret monazite ages with respect to the part of the thermal history (prograde, peak, cooling), which they represent.

An area crucial for this kind of study is the Teplá Crystalline unit (TCU) in the northwestern Bohemian Massif, where Cadomian (ca. 650–500 Ma) basement has been overprinted by Variscan (ca. 400–300 Ma) regional metamorphism. Here, the effects of Variscan reworking on the U–Pb systematics in monazite can be studied in detail, which provides important constraints on the factors and processes that influence the formation and resetting of monazite within the paragneisses of this area. Our approach is the combination of high-precision isotope dilution–thermal ionisation mass spectrometry (ID-TIMS) with chemical in situ dating by electron microprobe analysis (EMPA). In contrast to the conventional ID-TIMS method, EMPA or the chemical dating method is based on the fact that monazites are generally very rich in Th and U, and thus also radiogenic Pb, so that concentrations of elemental Th and Pb can be determined in situ by EMPA. Assuming that the monazites have no or very little common Pb, the elemental Pb should contain only the radiogenic ^{206}Pb, ^{207}Pb, ^{208}Pb isotopes that had formed by decay of ^{238}U, ^{235}U, and ^{232}Th, respectively. This method is very rapid compared to TIMS, inexpensive, ideally non-destructive, and with a microprobe beam of about 5 μm in diameter grains are analysed in situ, thus in microstructural context. The method, however, lacks the precision of conventional TIMS analyses, 2σ errors of one analysis are around 30 Myr, and so a statistical treatment of a larger set of single point analyses is necessary to reduce the errors. A more detailed description and discussion of the basics of the chemical Th–U–Pb method is given by Suzuki et al. (1991), Montel et al. (1996), Cocherie et al. (1998), and Scherrer et al. (2000). The EMP analyses are intended to complement the high-precision TIMS data, for which entire grains or parts of grains are dissolved, and which lack the spatial resolution so important to study the causes of discordance of analysed monazite grains. The results of this study have important implications not only for the geological history of this part of the Bohemian Massif, but also for the U–Pb systematics in monazite, mainly with respect to the processes of monazite formation and resetting.

Geological situation

Teplá Barrandian unit and Mariánské Lázně Complex

The Teplá Barrandian unit (TBU) in the central Bohemian Massif is part of the internal zone of the Variscan orogen of Central Europe (Fig. 1). It is surrounded in the northwest and along its southern borders by the high-grade metamorphic rocks of the Saxothuringian and the Moldanubian units, respectively. The Barrandian syncline in the central-eastern TBU comprises weakly unmetamorphosed sediments and volcanics of Cambrian to middle Devonian age that unconformably overlay upper Proterozoic rocks, the latter representing an active plate margin in which oceanic crust, island arc-type rocks, and synorogenic sediments (Cadomian flysch) were accreted (e.g. Kettner 1917; Fiala 1948; Waldhausrová 1984; Chlupác 1993). As a result of late Cadomian and Variscan crustal tilting, the lower crustal levels are exposed in the western TBU. The Cadomian basement here consists mainly of the Upper Proterozoic Kralupy–Zbraslav Group, including metagreywackes, metapelites, and -psammites, with intercalations of felsic and basic volcanics of MORB-like to alkaline geochemistry, cherts, and (black) shales (e.g. Mašek 1994; Chaloupský et al. 1995; Waldhausrová 1997). The maximum age for deposition is constrained by U–Pb data from magmatic pebbles of a metaconglomerate of the overlying Štěchovice Group giving 585 ± 7 and 568 ± 3 Ma (Dörr et al. 2002).

Due to exposure of progressively lower structural levels in the western TBU, the metamorphic grade increases from prehnite–pumpellyite facies in the Barrandian syncline (Cháb et al. 1995) to greenschist facies and upper amphibolite facies in the northwest and southwest of the TBU, in both areas displayed by Barrovian-type metamorphic zones. Eclogite facies rocks occur dominantly within the intermediate to mafic rocks of the adjacent Mariánské Lázně Complex (MLC), which represents a mixture of ca. 540 Ma-old oceanic rocks juxtaposed at depth with the lower crustal rocks of the structurally overlying TBU (Timmermann et al. 2004). Eclogitic lenses are also found within the northwesternmost TBU (e.g. Kastl and Tonika 1984; Cháb and Žáček 1994).

The Cadomian regional metamorphism is manifested especially in the southwestern TBU, the Domažlice crystalline complex (DCC; Zulauf 1997a). Paragneisses here were affected by both medium pressure (St-zone ≤ 7.5 kbar/450–570°C) and low pressure (LP) metamorphism (St/Ky-zone ≤ 5 kbar/550–650°C). The Cadomian event was accompanied by two deformation episodes (D1, D2). The latter D2 deformation, characterised by top-to-the-north mylonitic shearing, was associated with the LP/HT metamorphism and dated by U–Th–Pb EMPA of monazite from 551 to 540 Ma (Zulauf et al. 1999).

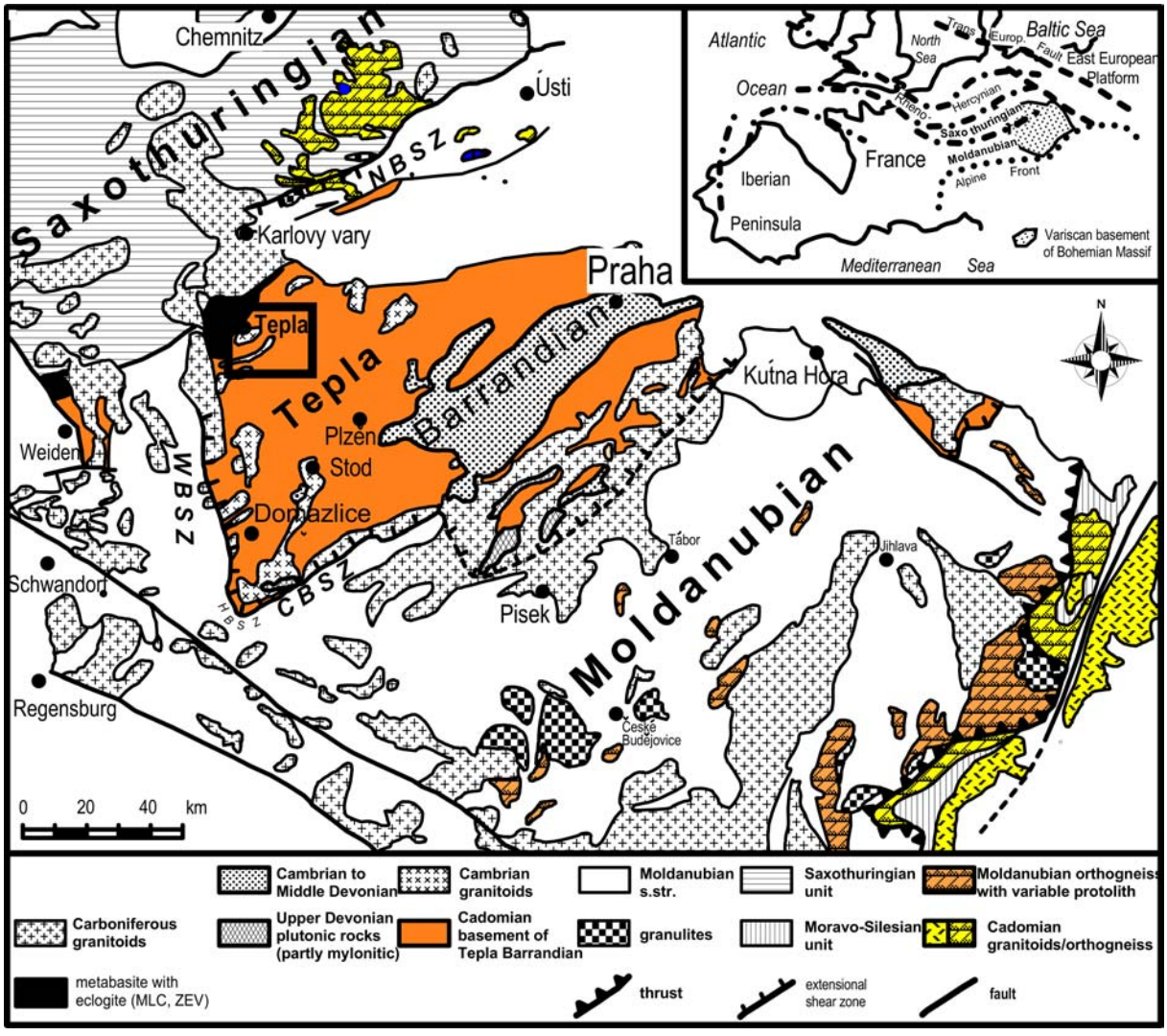

Fig. 1 Geological map showing position of the Teplaá Barrandian unit (*TBU*) in the central Bohemian Massif after Zulauf et al. (2002). *NBSZ* North Bohemian shear zone, *WBSZ* West Bohemian shear zone, *HBSZ* Hoher Bogen shear zone, *CBSZ* Central Bohemian shear zone

The Variscan orogeny was initiated by southeastward subduction of an ocean separating the Saxothuringian and the Teplá Barrandian, with final collision of both units causing significant crustal stacking (e.g. Franke 1989; Matte et al. 1990). The resulting regional metamorphism can be studied in the TCU in the northwestern TBU (Fig. 2), where approximately NE–SW running metamorphic isograds (chlorite–sericite, biotite, garnet, staurolite, kyanite) are exposed due to late Variscan crustal tilting (Záček et al. 1993; Cháb and Žáček 1994; Záček 1994; Cháb et al. 1997; Zulauf 2001). The Variscan event was accompanied by intense mylonitic D3 deformation. However, relics of the earlier, Cadomian D1 and D2, deformation episodes can still be found, for example as internal foliations in garnet or even as dominant foliation (S2) in the lower grade rocks of the chlorite–sericite, biotite, and garnet zones of the TCU (e.g. Zulauf 1997a; Zulauf and Vejnar 1998). Furthermore, the paragneisses of the TCU host two compositionally and texturally different garnet generations (Záček 1994; Zulauf 1997a). The earlier garnet generation (GrtI) is of Cadomian age; it grew between D1 and D2 under *P–T* conditions of 4–7 kbar and 480–570°C (Grt-zone). The second, Variscan, garnet generation (GrtII) grew under higher pressures of 6.1–7.5 kbar but similar temperatures of 520–570°C (Grt-zone; Zulauf 1997a).

In between the Cadomian and Variscan events, granitoid plutons intruded into the dominantly NE–SW dextral shear zones in the TCU, the transtensional regime being associated with the break-up of the northern Gondwana margin (e.g. Dörr et al. 1998; Zulauf and Vejnar 1998). The Lestkov, Hanov, and Teplá granitoids of the TCU were dated as middle Cambrian (516–511 Ma; Dörr et al. 1998), slightly younger compared to the plutons in the DCC (523 Ma; Zulauf et al. 1997) and

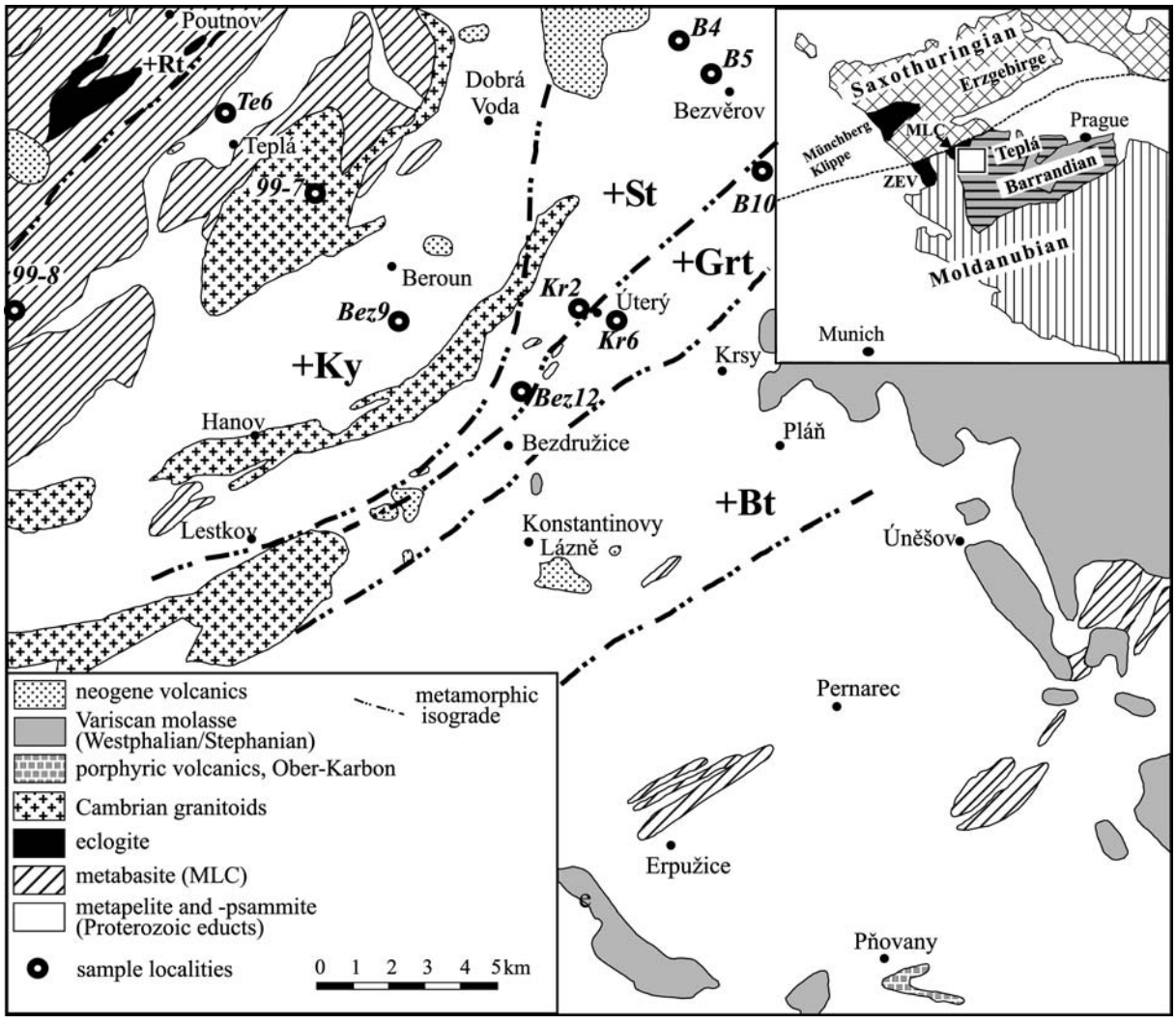

Fig. 2 Schematic geological map of the Teplá Crystalline unit (*TCU*) in the northwestern TBU and the southwestern Mariánské Lázně complex (*MLC*; after Zulauf 1997a). Sample localities (of the HT-set) are represented by *black circles*. + *Bt* Biotite zone, + *Grt* garnet zone, + *St* staurolite zone, + *Ky* kyanite zone. *Inset* shows location of study area within the Bohemian Massif

the Stod-Neukirchen Kdyně complex (524–522 Ma; Dörr et al. 2002). The plutons were affected only by the younger deformational phase (D3), thus supporting the geochronological evidence for their post-Cadomian emplacement (Zulauf 1997a). Contact metamorphism resulting from granitoid emplacement triggered static growth of prismatic sillimanite, large biotite and muscovite crystals, and locally cordierite; these phases were used to distinguish preplutonic and postplutonic assemblages in this area (Zulauf 1997a; and references therein). Widespread pegmatite emplacement in the TCU happened slightly later from 487 to 475 ± 5 Ma (Rb–Sr; U–Pb; Glodny et al. 1998). The recrystallisation of muscovite within the pegmatites was dated at 375–372 ± 4 Ma and taken to reflect Variscan deformation (Rb–Sr; Glodny et al. 1998). These ages coincide with K–Ar and $^{40}Ar/^{39}Ar$ mica ages from 383 to 366 Ma (Dallmeyer and Urban 1994; Zulauf 1997a; and references therein); however, U–Pb ages for Variscan regional metamorphism in the TCU did not exist until this study.

Located to the northwest of the TCU is the allochthonous intermediate to mafic MLC. Although the MLC is generally interpreted as a dismembered Cambro-Ordovician ophiolite complex affected by Variscan subduction (e.g. Kastl and Tonika 1984; Bowes and Aftalion 1991; Beard et al. 1995; Jelínek et al. 1997; and references therein), new studies indicate late Cadomian protolith ages for the main MLC rock association (Timmermann et al. 2004). The MLC comprises different thrust-bounded rock units with varying grades in deformation and metamorphism that generally dip to the southeast (e.g. Zulauf 1997b; and references therein). These include serpentinised peridotites, lower and higher grade amphibolites, latter with eclogite lenses, high-pressure granulites, coronitic metagabbros, and intercalations of paragneisses and felsic orthogneisses (Jelínek et al. 1997; and references therein). Field

relationships such as inclusions of amphibolite in the metagabbros or intrusion of metagabbros into the orthogneisses of the TCU indicate that the suite of metagabbros, located at the southeastern boundary of the MLC and in trains within the northwestern kyanite zone of the TCU, is younger than the amphibolites of the MLC (e.g. Kastl and Tonika 1984; Štědrá et al. 2002). A minimum age for the metagabbros is given by an upper intercept age of 496 ± 1 Ma for a weakly deformed gabbro pegmatite, interpreted to reflect the beginning rifting event that leads to the separation of microplates along the northern Gondwana margin (Bowes and Aftalion 1991).

Characteristics of sample localities

The paragneiss samples analysed for monazite U–Pb geochronology originate from the garnet, staurolite, and kyanite zones of the TCU (Fig. 2, Table 1).

The *garnet zone* reflects the appearance of the first generation garnet (GrtI) within the micaschists and metagreywackes (Záček 1994). Relics of the older Cadomian metamorphism and deformation are found in the analysed samples HT-B10 and HT-Kr6. The early S1 foliation (± sigmoidal) is present as internal structure in garnet I, whereas the dominant mylonitic foliation and N–S trending mineral lineation is associated with the late Cadomian D2 deformation and greenschist facies metamorphism (Zulauf 1997a). Moderate Variscan reworking resulted in NW-directed recumbent folds (F3) and in a typical NE–SW trending crenulation lineation, both associated with D3. Furthermore, garnet II, differing structurally (inclusion-rich) and chemically (Ca-richer) from garnet I, overgrows the S2 foliation (Záček 1994).

The *staurolite zone* is characterised by the occurrence of both pre- and postplutonic staurolite (Záček 1994). Analysed samples from this zone are HT-B4-1, a pelitic, biotite-rich layer of a mylonitic paragneiss, Grt-St micaschists HT-B5, Grt-St micaschist HT-Kr2-1, and Bez12 (Table 1). Cadomian fabrics within the samples are restricted to rare internal S1 foliations in garnet and staurolite (I) and relics of S2 foliation in garnet and staurolite (II) (Zulauf 1997a). D2 metamorphism happened under epidote–amphibolite facies conditions

Table 1 Sample localities, Teplá crystalline unit (TCU) and Mariánské Lázně Complex (MLC), Czech Republic

Sample no.	Locality	Rock type/mineral assemblage	Comments
HT-B10 TCU	Roadcut east of Dolni Jamné	Paragneiss Qtz-Pl-Ms-Bt-Grt-Chl-Op	Grt-zone (greenschist facies), N–S Cadomian mineral lineation, GrtI core(D2): 5.5–6.8 kbar/510–550°, GrtI rim: 5–6.2 kbar/550–590° (Zulauf 1997a) NW–SE Variscan lineation, Variscan folding
HT-Kr6 TCU	Roadcut, northwest exit of Olešovice	Paragneiss Qtz-Pl-Ms-Bt-Grt-Chl-Op	Grt-zone, Cadomian metamorphism, weak Variscan (≤ 450°C) overprint and deformation
Bez12 TCU	Roadcut 1 km north of Bezdružice, near site of Český Ml.	Grt-St micaschist Qtz-Pl-Ms-Bt-Grt-St-Op	St-zone, degree of Variscan overprint onto Cadomian metamorphism unclear!
HT-Kr2 TCU	Roadcut at west exit of Uterý	Mica-rich greywacke Qtz-Pl-Ms-Bt-Grt-St-Op	St-zone, Cadomian or Variscan? Macroscopic S1 foliation between the planes of the dominant Cadomian S2 foliation[a], SE dipping S2 foliation (30–50°), N–S stretching lineation (D2)
HT-B5 TCU	Roadcut between Třebouň and Bezvěrov	Grt-St paragneiss/micaschist Qtz-Pl-Ms-Bt-Grt-St-Chl-Op	St-zone (amph. facies), GrtI (preplutonic): 3.5–5.8 kbar/520–580° (Zulauf 1997a), strong Variscan overprint: GrtII: 6–8 kbar/540–600° (Zulauf 1997a)
HT-B4-1 TCU	Carpark at the E49 between Třebouň and Bezvěrov	Pelitic, biotite-rich layer of mylonitic paragneiss Qtz-Pl-Ms-Bt-Grt-St ± Sil-Chl-Op	St-zone (amph. facies), strong Variscan overprint
HT-Bez9	Roadcut between Stare Sedlo and Zahrádka	High-grade metagreywacke Qtz-Pl-Ms-Bt-Grt ± St-Ky-Chl-Op	Ky-zone, (Variscan?) amphibolite facies, retrograde Ms due to contact metamorphism
HT-Te6 TCU	Open quarry northwest of Teplá (between road and railway)	High-grade mylonitic paragneiss Qtz-Pl-Ms-Bt-Sil ± Grt-Chl-Op	Near MLC, Sil, no Ky, no St, NW–SE lineation
HT-99-7 TCU	Ovčidvůr shipyard	Medium to coarse grained coronitic metagabbro	Structurally below one of important shear zones in TCU
HT-99-8 MLC	N of Pistov	Garnet-bearing metabasite, distinct ~N–S stretching lineation (older than NW–SE lineation?)	Protolith age compared to metagabbro in TCU and Münchberg Massif?

Mineral abbreviations follow Kretz (1983)
[a]Zulauf (2001)

(Zulauf 1997a). Subsequent static growth of biotite and muscovite (in HT-Kr2-1 also staurolite) perpendicular to the S2 foliation possibly results from contact metamorphism associated with the nearby intrusion of the Hanov orthogneiss (Zulauf 1997a; Dörr et al. 1998). Later Variscan convergence (D3) caused intense mylonitic reworking, with garnet II typically growing in the pressure shadows of garnet I, indicating NW–SE directed stretching (Zulauf 1997a). Peak conditions in the central staurolite zone are up to 9 kbar and ca. 600°C (Zulauf 1997a).

The *kyanite zone* hosts both preplutonic as well as postplutonic kyanite, whereas the dominant garnet is of the second generation (Grt II) (Záček 1994). The samples analysed from this area are a high-grade metamorphic greywacke (HT-Bez9) and a migmatitic paragneiss (HT-Te6). HT-Te6 originates from the northwesternmost part of the TCU (Fig. 2), adjacent to the MLC, here represented by a suite of metagabbros (e.g. Štědrá et al. 2002). As the rocks of the kyanite zone experienced the strongest reworking during the Variscan D3 event, pre-D3 structures are generally absent (Zulauf 1997a). In contrast, widespread evidence for Middle Cambrian contact metamorphism includes statically grown coarse biotite and muscovite (e.g. HT-Bez9), fibrolitic and prismatic sillimanite, and cordierite later replaced by Variscan staurolite (Cháb and Žáček 1994; Zulauf 1997a). The Variscan D3 event is manifested in the paragneisses by penetrative mylonitisation (S3 foliation), with kinematic indicators indicating top-to-the-WNW shearing (Zulauf 1997a). Metamorphism happened under at least amphibolite facies conditions (5–8.7 kbar, 550–645°C; Cháb and Žáček 1994). Syn-D3 growth of sillimanite is restricted to the northwestern kyanite zone close to the MLC (HT-Te6; Zulauf 1997). In addition, during Variscan regional metamorphism, andalusite within the Ordovician pegmatite is locally replaced by kyanite (Záček 1994).

The metagabbros of the MLC exhibit a relict ophitic to coronitic fabric. Preserved igneous minerals are partly recrystallised plagioclase, ortho- and clinopyroxene, hornblende, olivine, and apatite. Conditions of primary equilibration were determined at 900°C and 16 kbar (Jelínek et al. 1997; and references therein), whereas Štědrá et al. (2002) proposes static recrystallisation under initial conditions of 600–730°C and 8–11 kbar. Subsequent metamorphism including first a pressure increase before amphibolitisation facilitated growth of additional metamorphic minerals (garnet, kyanite, zoisite, rutile, ilmenite, titanite, magnetite, quartz; retrograde actinolite, epidote, oligoclase, chlorite, calcite; Jelínek et al. 1997; and references therein). A trace element study of MLC and TBU metagabbros indicates geochemical characteristics typical of within-plate magmatism (Štědrá et al. 2002; Timmermann et al. 2004). The composition of metagabbros could also be associated with a rift-related setting, as suggested by Štědrá et al. (2002). The minimum age of the metagabbros is constrained by the upper intercept age of 496 ± 1 Ma from the gabbro pegmatite close to the locality of HT-99-8 (Fig. 2; Bowes and Aftalion 1991). Coronitic metagabbro HT-99-7 was taken from an outcrop structurally below sheared porphyritic Teplá orthogneiss dated 513 +7/−6 Ma (U–Pb zircon upper intercept age; Dörr et al. 1998). Sample HT-99-7 (Pl-Cpx-Hbl-Bt-Ilm-Grt-Ap-Zoi) is medium to coarse grained, with an ophitic texture attributed to the relict plagioclase laths. Garnet growth during subsequent metamorphism (Štědrá et al. 2002) is manifested mainly by isolated monocrystals along clinopyroxene margins at the expense of plagioclase. Pale grey, medium-grained HT-99-8 originates from a garnet-bearing metabasite in the southern MLC (Fig. 2). The sample exhibits a relict igneous texture and continuous garnet coronas around the mafic minerals such as clinopyroxene, amphibolite, and ilmenite. Relict, colourless orthopyroxene occurs in the centre of clinopyroxene–biotite–hornblende aggregates. Metamorphic kyanite is rare, whereas Na-rich clinopyroxene/omphacite is absent.

Analytical techniques

Samples for ID-TIMS were processed at the IGL of the University of Giessen using standard mineral separation techniques. These include crushing and sieving, before concentration of heavy minerals by heavy liquids (bromoform, methyleneiodide) and magnetic separation with a Frantz isodynamic separator. Monazite grains, the size of 20–350 µm, were handpicked from the 0.6–1.0 A fraction of the heavy mineral separate of each sample for ID-TIMS analyses and for polished grain mounts for EMPA. For the latter, monazite grains were embedded in epoxy resin and, after epoxy hardening, ground down to approximately half of their initial thickness and polished. After washing with 2N HNO_3 and acetone, monazite grains were weighed and transferred to 5 ml Savillex beakers before adding a mixed $^{205}Pb/^{235}U$ spike. Monazites were dissolved in 6N HCl on a hot plate at ca. 80°C for 3 days. After evaporation to dryness the sample was converted by adding 0.5 ml 3N HCl. Subsequent chemical extraction of Pb and U was carried out with 400 µl columns containing an ion-exchange resin (Dowex AG 1×8, 100–200 mesh) in a stepwise elution process after Manhès et al. (1979). From metagabbro samples HT-99-7 and HT-99-8, zircons were handpicked from the non-magnetic fraction of the heavy mineral separate, abraded with pyrite for 6 h (Krogh 1982), and washed with HNO_3 and 2N HCl in an ultrasonic bath. Zircons were weighed and loaded with 24N HF and a mixed $^{205}Pb/^{235}U$ spike into small Savillex vials, which were then placed into a Parr bomb (Parrish 1987). After dissolution at 180°C for 48 h and subsequent evaporation to dryness at ca. 80°C on a hotplate, the sample

Table 2 U–Pb monazite and zircon data from the TCU and MLC, Czech Republic

Sample fraction[a]	wt[b] (mg)	U (ppm)	Pb[c] (ppm)	Pb[d] (ppm)	Th/U[e]	$^{206}Pb^{f}/^{204}Pb$ (Ma)	$^{206}Pb^{g}/^{238}U$ (Ma)	$^{207}Pb^{g}/^{235}U$ (Ma)	$^{207}Pb^{g}/^{206}Pb$ (Ma)	$^{206}Pb^{h}/^{238}U$ (Ma)	$^{207}Pb^{h}/^{235}U$ (Ma)	Corr. coeff. (Ma)	$^{207}Pb^{h}/^{206}Pb$ (Ma)
(a) Paragneisses TCU													
HT-Te6													
Mnz1;160×160	0.01	5,655	556	4.0	1.25	7,068	0.07920 ± 0.55	0.6332 ± 0.66	0.05799 ± 0.37	491	498	0.83	529 ± 8
Mnz2; 180×160	0.023	1,450	188	0.7	2.65	10,620	0.08030 ± 0.14	0.6337 ± 0.19	0.05724 ± 0.12	498	498	0.77	501 ± 3
Mnz3; 180×120	0.01	4,376	502	2.3	1.99	9,556	0.07958 ± 0.19	0.6271 ± 0.21	0.05715 ± 0.09	494	494	0.9	497 ± 2
Mnz4; 130×115	0.01	3,005	368	3.9	2.36	3,869	0.07957 ± 0.17	0.6277 ± 0.22	0.05722 ± 0.13	494	495	0.81	500 ± 3
Mnz5; 70×100	0.01	805	113	1.6	3.34	2,462	0.07846 ± 0.28	0.6252 ± 0.44	0.05779 ± 0.33	487	493	0.67	522 ± 7
Mnz6; 20–30 (8)	0.01	373	60	2.9	4.95	603	0.07230 ± 0.64	0.5584 ± 1.57	0.05602 ± 1.41	450	450	0.44	453 ± 31
Mnz7; 25–40 (5)	0.01	219	36	1.3	5.02	761	0.07314 ± 1.00	0.5830 ± 1.51	0.05781 ± 1.1	455	466	0.69	523 ± 24
Mnz8; 20–40 (8)	0.01	179	28	14.6	5.77	70	0.06776 ± 1.14	0.5308 ± 5.54	0.05682 ± 5.29	423	432	0.31	485 ± 120
Mnz11; 180×100	0.015	3,802	461	8.8	2.40	2,132	0.07843 ± 0.20	0.6185 ± 0.28	0.05719 ± 0.18	487	489	0.75	499 ± 4
Mnz13; 200×100	0.01	4,391	565	12.2	2.78	1,776	0.07814 ± 0.37	0.6157 ± 0.46	0.05715 ± 0.27	485	487	0.81	497 ± 6
Mnz16; 100×64	0.01	576	15	0.8	5.76	500	0.01059 ± 6.00	0.0822 ± 6.76	0.05631 ± 3.03	68	80	0.89	465 ± 67
Mnz17; ≤ 40 (7)	0.01	2,080	117	14.7	2.38	351	0.03779 ± 3.32	0.2932 ± 3.78	0.05627 ± 1.75	239	261	0.89	463 ± 39
Mnz18; ≤ 40 (8)	0.01	1,066	85	5.9	4.32	457	0.03891 ± 3.44	0.3080 ± 5.28	0.05742 ± 3.99	246	273	0.65	508 ± 88
Mnz21; 200×260	0.018	11,304	1,727	3.3	3.72	17,356	0.0800 ± 0.17	0.6296 ± 0.18	0.05706 ± 0.06	496	496	0.95	494 ± 1
Mnz22; 160×160	0.01	10,687	1,328	4.1	2.45	12,938	0.07921 ± 0.27	0.6247 ± 0.29	0.05719 ± 0.08	491	493	0.96	499 ± 2
Mnz25; 250×160	0.015	12,340	1,603	5.4	2.67	11,481	0.07986 ± 0.14	0.6281 ± 0.15	0.05704 ± 0.07	495	495	0.89	493 ± 2
Mnz30;30–60(22)	0.015	1,640	227	93.0	4.42	96	0.07093 ± 0.64	0.5355 ± 9.37	0.05476 ± 9.15	442	435	0.38	402 ± 200
HT-B10													
Mnz3; ≤ 64 (3)	0.01	671	92	0.003	4.68	979	0.06143 ± 0.41	0.4585 ± 1.06	0.05413 ± 0.96	384	383	0.43	376 ± 21
Mnz5; 60×40 (3)	0.01	372	55	0.003	4.98	456	0.06186 ± 0.67	0.4773 ± 1.90	0.05596 ± 1.74	387	396	0.41	450 ± 39
Mnz6; ~ 64 (6)	0.01	652	92	0.001	5.01	2,056	0.06183 ± 0.41	0.4662 ± 0.78	0.05469 ± 0.65	387	389	0.56	399 ± 15
Mnz7; ≤ 60 (3)	0.01	299	39	0.001	4.48	1,524	0.06122 ± 0.86	0.4661 ± 1.32	0.05521 ± 0.96	383	388	0.68	421 ± 21
HT-B5													
Mnz3; ≤ 40 (4)	0.01	364	46	0.55	4.22	2,596	0.06177 ± 0.73	0.4828 ± 1.26	0.05668 ± 1.00	386	400	0.61	479 ± 22
HT-B4-1													
Mnz2; ~64, (2)	0.01	526	72	0.93	4.93	2,190	0.06090 ± 1.02	0.4652 ± 1.62	0.05540 ± 1.23	381	388	0.66	428 ± 27
Mnz3; 60×100	0.01	359	57	2.21	6.20	643	0.06127 ± 1.06	0.48095 ± 2.05	0.05693 ± 1.71	383	399	0.55	489 ± 38
HT-Bez9													
Mnz3; 40×40	0.01	156	19	1.04	4.14	591	0.06103 ± 1.61	0.4335 ± 2.47	0.05151 ± 1.8	382	366	0.69	264 ± 41
(b) Metagabbros MLC													
HT-99-7													
Zir 2066;	0.01	1,062	86	6.4	0.52	839	0.07977 ± 0.18	0.6313 ± 0.90	0.05740 ± 0.86	495	497	0.3	507 ± 19
Zir 2349; brown	0.056	789	62	0.4	0.36	10,655	0.07769 ± 0.40	0.6152 ± 0.49	0.05743 ± 0.29	482	487	0.81	508 ± 6
Zir 2351; (4)	0.096	512	40	0.2	0.34	10,760	0.07847 ± 0.20	0.6198 ± 0.25	0.05729 ± 0.16	487	490	0.78	503 ± 4
Zir 2353; (9)	0.08	369	30	0.5	0.37	3,942	0.07899 ± 0.28	0.6268 ± 0.4	0.05755 ± 0.29	490	494	0.70	513 ± 6
HT-99-8													
Zir 2069	0.027	121	11	0.8	1.07	819	0.08013 ± 0.32	0.6419 ± 0.99	0.05811 ± 0.92	497	504	0.38	534 ± 20
Zir 2071	0.018	297	27	1.3	0.79	1,203	0.08121 ± 0.21	0.6465 ± 0.68	0.05773 ± 0.63	503	506	0.38	520 ± 14
Zir 2344; (8)	0.035	163	16	0.4	1.04	2,137	0.08061 ± 0.52	0.6414 ± 1.24	0.05771 ± 1.12	500	503	0.43	519 ± 25

Table 2 (Contd.)

Sample fraction[a]	wt[b] (mg)	U (ppm)	Pb[c] (ppm)	Pb[d] (ppm)	Th/U[e]	$^{206}Pb^{f}/^{204}Pb$ (Ma)	$^{206}Pb^{g}/^{238}U$ (Ma)	$^{207}Pb^{g}/^{235}U$ (Ma)	$^{207}Pb^{g}/^{206}Pb$ (Ma)	$^{206}Pb^{h}/^{238}U$ (Ma)	$^{207}Pb^{h}/^{235}U$ (Ma)	Corr. coeff. (Ma)	$^{207}Pb^{h}/^{206}Pb$ (Ma)
Zir 2345; (9)	0.05	333	34	0.8	1.24	2,226	0.07983 ± 0.44	0.6356 ± 0.96	0.05776 ± 0.85	495	500	0.47	521 ± 19
Zir 2346; (3)	0.027	434	42	0.5	0.99	4,718	0.08098 ± 0.23	0.6403 ± 0.52	0.05735 ± 0.46	502	503	0.46	505 ± 10
Zir 2348; (9)	0.049	161	16	0.5	1.13	1,746	0.08040 ± 0.47	0.6372 ± 0.91	0.05748 ± 0.77	499	501	0.53	510 ± 17

[a] *Mnz* Monazite; *Zir* zircon; approximate size given in µm. Brackets give number of grains in multigrain fractions, except for (b), all of which analyses constitute multigrain fractions
[b] Maximum errors are ±50% for weights <0.002 mg and ±20% for weights >0.002 mg
[c] Radiogenic Pb
[d] Total common Pb in analyses corrected for fractionation and spike
[e] Model ratio calculated from $^{208}Pb/^{206}Pb$ ratio
[f] Measured ratio, corrected for mass discrimination (0.1 ± 0.03‰), 205Pb spike, and blank contribution (0.01 ± 0.005 ng for monazite, 0.005 ± 0.0025 ng for zircon)
[g] Common Pb correction for blank Pb and U, and Stacey and Kramers (1975) model Pb composition equivalent to the interpreted age of the individual grains. Errors are two standard errors of the mean in percent for ratios
[h] Corrected for blank and common Pb; errors are two standard errors of the mean when expressed in Ma

was converted into chloride by adding 0.2 ml 3N HCl. Chemical separation of Pb and U on 100 µl columns (ion-exchange resin AG 1×8, 100–200 mesh) followed the method of Krogh (1973). The U and Pb isotope ratios of monazite and zircon were obtained at the IGL using a Finnigan MAT 261 mass spectrometer in static multicollector mode with simultaneous ion counting of ^{204}Pb, and for samples of low radiogenic Pb content in dynamic peak jumping mode (for detailed procedure see Dörr et al. 2002). All isotopic ratios are corrected for mass fractionation (1.0 ± 0.3‰/a.m.u), blank (≈10 pg for monazite and 5 pg for single zircon) and initial lead using Stacey and Kramers (1975) model Pb composition. The U–Pb data were calculated using the program PBDAT (Ludwig 1980), the isotope ratios were plotted using Isoplot (Ludwig 2001), with error ellipses reflecting 2σ uncertainty. The concordia curves are plotted with decay-constant errors. Analytical data are presented in Table 2.

Electron microprobe analyses were carried out at the University of Salzburg using a Jeol JX 8600, with operating conditions of 15 kV, 250 nA, and a beam size of 5 µm (for details concerning element lines and standards see Finger and Helmy 1998). For Pb (Mα) counting times were 480 s on peak and 2×240 s on background. Counting times for the Th (Mα) and U (Mα) were 30 s (2×15 s) and 50 s (2×25 s), respectively. All other elements have been determined with 10 s per analysis on peak and 2×5 s on background. The 2σ errors as resulting from the counting statistics of the microprobe under the chosen analytical conditions were typically ±0.04–0.05 wt% for the Th, ±0.02–0.03 wt% for U and ±0.007 wt% for the Pb. Chemical profiles of monazite from sample HT-Te6 were recorded with a maximally focused beam (ca. 1–2 µm diameter) to obtain a better spatial resolution. In order to avoid damage of the sample and the carbon coating, respectively, counting times had to be reduced in these cases to roughly half, resulting in a correspondingly higher error. In contrast, brightness of main spots (e.g. Fig. 7) is due to some limited damage to the crystal by the electron beam, as several measurements were carried out with a defocused beam with an overall duration of at least 0.5 h. Final elemental concentrations were derived using a ZAF correction program. Small Y and Th interferences on the Pb Mα line and a Th interference on the U Mα line were routinely corrected. For each single analysis a chemical model age was calculated after equations of Montel et al. (1996). Th* values were recalculated with model ages after Suzuki et al. (1991). The accuracy of the dating procedure was controlled by means of the monazite age standard F5 (Finger and Helmy 1998). EMP analyses were carried out on monazite in (a) polished sections, in order to have a microstructural control on the location of monazites with respect to the ages of mineral assemblages and (b) in grain mounts from the same heavy mineral separate as the monazite taken for ID-TIMS analyses. The results of EMPA dating are presented in Table 3.

Table 3 Chemical characteristics, Th, U, Pb contents (wt% elements), Th* values, and model ages (95% confidence level) of analysed monazite from TCU-paragneisses

Sample	Size (μm)	Grain boundary	Position	Zoning	La_2O_3	Nd_2O_3	Y_2O_3	ThO_2	UO_2	Th	U	Pb	Th*	Age (Ma)
Garnet-zone														
HT-B10 (polished section)														
m1	30/10	Polygonal	Incl.(mica)		12.55	12.65	0.96	2.95	0.77	2,594	0.681	0.083	4,816	384 ± 26
m3-A	20/20	Polygonal	Pl-Kfs	Bright	12.59	12.57	0.45	3.72	1.22	3,266	1.074	0.117	6,775	387 ± 39
m3-B	20/20	Polygonal	Pl-Kfs	Dark	12.58	12.69	1.32	3.17	0.63	2,785	0.552	0.088	4,593	431 ± 38
m4-A	30/30	Polygonal	Mica–feldspar	Dark	12.44	12.68	1.33	3.06	0.71	2,690	0.624	0.075	4,722	357 ± 26
m4-B	30/30	Polygonal	Mica–feldspar	Bright	13.06	12.26	0.17	4.21	1.08	3,703	0.952	0.111	6,807	364 ± 37
m5	20/20	Polygonal	Mica–feldspar		12.35	12.38	0.72	4.26	0.90	3,744	0.793	0.098	6,327	347 ± 28
Weighted average													(MSWD = 3.2)	373 ± 29
HT-Kr6 (polished section)														
m1	40/10	Polygonal	Mica–feldspar		12.82	12.26	0.56	3.53	0.79	3,101	0.695	0.091	5,370	380 ± 33
m2-A	80/30	Lobate	Mica–feldspar	Core	12.19	12.00	0.93	4.67	0.74	4,103	0.649	0.109	6,222	392 ± 29
m2-B	80/30	Lobate	Mica–feldspar	Rim	12.58	12.19	1.06	3.71	0.74	3,264	0.656	0.088	5,402	365 ± 33
m3	60/20	Lobate	Mica–feldspar	core	13.12	12.00	0.28	3.94	0.92	3,461	0.812	0.097	6,106	358 ± 29
m4	40/20	Polygonal–lobate	Incl.(mica)		12.22	12.22	1.13	4.00	0.76	3,519	0.667	0.093	5,694	367 ± 32
m5	50/10	Polygonal	Incl.(fsp)		12.75	12.18	0.76	3.80	0.74	3,340	0.653	0.094	5,473	386 ± 33
Weighted average													(MSWD = 0.78)	375 ± 13
Staurolite-zone														
Bez12 (polished section)														
m2	20/10	Polygonal	Mica–feldspar	Bright core	12.58	12.31	1.30	2.45	0.52	2,157	0.454	0.080	3,651	489 ± 49
m3-A	40/10	Polygonal	Incl.(mica)	Dark	12.24	12.04	0.88	3.98	1.06	3,497	0.933	0.118	6,547	404 ± 27
m3-B	40/10	Polygonal	Incl.(mica)	Bright	12.21	12.05	1.13	3.71	0.81	3,258	0.715	0.121	5,612	483 ± 32
m4	30/10	Lobate-amoeboid	Mica–feldspar		12.01	11.98	1.44	3.51	0.81	3,085	0.716	0.095	5,425	393 ± 33
HT-Kr2-1a (polished section)														
m1	50/10	Polygonal–lobate	Incl.(mica)		12.16	12.59	2.03	4.02	0.98	3,529	0.862	0.110	6,343	389 ± 28
m2	20/20	Polygonal	Mica–feldspar		12.75	12.46	1.03	3.25	0.78	2,858	0.684	0.090	5,092	396 ± 35
m3	20/20	Polygonal–lobate	Incl.(fsp)		11.75	11.83	1.54	3.58	1.14	3,148	1.007	0.093	6,421	326 ± 28
m4	20/20	Polygonal–lobate	Incl.(mica)		12.57	12.55	1.94	3.01	0.97	2,647	0.851	0.095	5,428	393 ± 33
m5	40/10	Polygonal–lobate	Incl.(fsp)		12.07	12.07	1.88	3.61	0.82	3,177	0.721	0.096	5,532	390 ± 32
Weighted average													(MSWD = 4.2)	376 ± 39
HT-Kr2-1 (polished section)														
m2	20/10	Lobate (interstitial)	Incl.(fsp)		12.05	12.11	1.53	3.62	0.73	3,185	0.644	0.083	5,284	353 ± #
m3	20/10	Lobate (interstitial)	Feldspar		12.77	13.59	1.29	1.89	0.45	1,658	0.398	0.060	2,965	456 ± 53
m4-A	30/10	Polygonal–lobate	Incl.(fsp)	Core	12.49	12.46	1.42	2.73	0.77	2,396	0.681	0.084	4,624	409 ± #
m4-B	30/10	Polygonal–lobate	Incl.(fsp)	Rim	12.63	12.62	1.51	2.56	0.64	2,253	0.562	0.083	4,099	453 ± 38
m5-A	30/20	Polygonal–lobate	Mica	Core	12.31	12.38	1.48	2.58	0.72	2,266	0.636	0.088	4,355	454 ± 36
m5-B	30/20	Polygonal–lobate	Mica	Rim	12.21	12.30	1.54	3.33	0.89	2,931	0.789	0.102	5,511	414 ± #
m5-C	30/20	Polygonal–lobate	Mica	Rim	12.02	12.26	1.59	3.11	0.79	2,733	0.697	0.089	5,010	397 ± 31
Weighted average													"young"	393 ± 45
Weighted average													"old"	454 ± 23
HT-B5 (grain mount)														
m1	< 40		–		11.93	12.88	1.74	3.78	1.09	3,322	0.960	0.104	6,451	362 ± 42
m2	< 40		–		12.97	12.64	0.46	4.36	1.12	3,835	0.989	0.114	7,059	362 ± 38
m3	< 40		–		12.68	12.69	0.67	4.79	1.01	4,208	0.892	0.125	7,121	393 ± 38
Weighted average													(MSWD = 0.88)	373 ± 22
HT-B4-1 (polished section)														
m1-A	80/30	Polygonal–lobate	Mica–feldspar	Core	12.51	12.70	1.70	2.11	0.74	1,857	0.653	0.066	3,987	370 ± 39
m1-B	80/30	Polygonal–lobate	Mica–feldspar	Rim	12.21	12.57	1.74	2.66	0.79	2,339	0.694	0.077	4,604	375 ± 34
m2-				Core	12.38	12.75	1.85	2.63	0.79	2,313	0.700	0.081	4,599	394 ± 39
m3-A	50/30	Polygonal	Incl.(mica)	Core	11.49	12.26	1.74	4.10	0.86	3,606	0.758	0.113	6,088	417 ± 26
m3-B	50/30	Polygonal	Incl.(mica)	Rim	11.63	12.43	1.85	3.90	0.85	3,431	0.746	0.101	5,868	385 ± 27
m4	100/40	Lobate	Mica–feldspar		11.73	12.68	1.83	3.81	0.84	3,353	0.740	0.087	5,760	339 ± 27
m5-A	150/20	Polygonal–lobate	Mica–feldspar	Core	12.23	12.80	1.67	2.51	0.67	2,202	0.593	0.079	4,145	428 ± 38
m5-B	150/20	Polygonal–lobate	Mica–feldspar	Core	11.76	12.72	1.64	3.76	0.73	3,302	0.640	0.097	5,394	401 ± 29
m6	150/20	Polygonal–lobate	Incl.(fsp)		11.78	12.53	1.76	3.69	0.92	3,244	0.811	0.099	5,890	378 ± 27
m7-A	150/20	Polygonal–lobate	Mica–feldspar	Core	11.37	12.35	2.02	4.17	1.08	3,666	0.949	0.109	6,759	363 ± 23
m7-B	150/20	Polygonal–lobate	Mica–feldspar	Core	11.84	12.45	1.69	3.37	0.74	2,959	0.655	0.087	5,097	382 ± 31
Weighted average													(MSWD = 2.9)	382 ± 17
Kyanite-zone														
HT-Bez9														
m1	60/10	Polygonal–lobate	Feldspar		13.20	11.44	1.01	4.22	0.86	3,710	0.757	0.100	6,179	363 ± 29
m2	50/20	Extreme polygonal	Gr. boundary		12.58	12.46	1.10	3.18	0.94	2,796	0.830	0.097	5,508	395 ± 33
m3-A	60/20	Polygonal–lobate	Mica–feldspar	Core	11.79	12.21	2.12	3.91	1.06	3,438	0.931	0.129	6,491	444 ± #
m3-B	60/20	Polygonal–lobate	Mica–feldspar	Rim	11.86	12.27	2.16	3.84	1.05	3,378	0.923	0.114	6,395	400 ± 28

Table 3 (Contd.)

Sample	Size (μm)	Grain boundary	Position	Zoning	La_2O_3	Nd_2O_3	Y_2O_3	ThO_2	UO_2	Th	U	Pb	Th*	Age (Ma)
m4	60/ < 10	Extreme polygonal	Mica–feldspar		11.87	12.43	1.78	3.41	0.85	2,994	0.749	0.082	5,432	339 ± 33
m5-A	20/10	Lobate	Incl.(mica)	Core1	11.58	12.51	1.81	3.18	0.96	2,795	0.843	0.087	5,541	354 ± 32
m5-B	20/10	Lobate	Incl.(mica)	Core2	12.04	12.54	1.46	3.27	0.93	2,876	0.818	0.094	5,545	380 ± 32
Weighted average (excl. m3-A)													(MSWD = 2.4)	373 ± 25
HT-Te6														
m1-A	60/20	Polygonal	Incl.(mica)	Core	12.43	13.20	1.45	4.24	0.54	3,727	0.478	0.114	5,300	479 ± 30
m1-B	60/20	Polygonal	Incl.(mica)	Rim	12.22	13.31	1.70	3.63	0.66	3,187	0.579	0.108	5,091	473 ± 31
m3-A	50/50	Polygonal–lobate	Mica–feldspar	Dark zone	11.72	12.88	1.98	1.87	1.64	1,645	1.449	0.135	6,409	473 ± 25
m3-B	50/50	Polygonal–lobate	Mica–feldspar	Bright zone	11.69	12.13	1.34	5.84	0.53	5,132	0.464	0.146	6,660	488 ± 23
m4	50/20	Polygonal	Incl.(fsp)		11.48	12.63	1.66	4.50	1.27	3,952	1.123	0.182	7,661	530 ± 20
m5-A	60/20	Polygonal–lobate	Incl.(mica)	Core	11.74	12.79	1.94	3.32	1.09	2,916	0.957	0.146	6,078	537 ± 26
m5-B	60/20	Polygonal–lobate	Incl.(mica)	Rim	12.06	12.69	1.81	3.48	1.02	3,057	0.897	0.101	5,985	380 ± 26
m8-A	80/50	Polygonal–lobate	Mica–feldspar	Bright core	11.42	12.05	1.42	6.12	0.46	5,381	0.402	0.145	6,704	483 ± 23
m8-B	80/50	Polygonal–lobate	Mica–feldspar	Dark rim	11.87	12.41	2.35	3.00	1.01	2,637	0.889	0.110	5,553	442 ± 28
m9-A	70/30	Polygonal–lobate	Mica–feldspar	Bright core	11.32	12.29	1.60	5.21	0.44	4,582	0.385	0.121	5,847	462 ± 27
m9-B	70/30	Polygonal–lobate	Mica–feldspar	Dark rim	11.22	12.47	2.47	3.48	1.05	3,061	0.925	0.121	6,094	446 ± 26

MSWD Mean standard weighted deviation

Results

ID-TIMS

Paragneisses TCU

Contrary to prior expectation, the paragneisses in the garnet and staurolite zones of the TCU contain only scarce monazite. Furthermore, the monazite present within some of the samples is commonly of unsuitable size (< 20 μm) for ID-TIMS analyses; therefore sample analyses for the most part of the TCU were restricted to four paragneisses (see below).

Only migmatitic paragneiss *HT-Te6* from the *kyanite zone* in the northwestern TCU next to the MLC (Fig. 2) contains abundant monazite in various grain sizes from ≤ 20 to 350 μm. There are three major groups of morphologies: (a) large grain sizes (> 100–350 μm), generally tabular, mostly euhedral, clear, of deep yellow colour and only minor cracks or inclusions; (b) small (20–40 μm), round, pale yellow grains; and (c) oval to round, tabular, dusty grey-yellow grains that are variably corroded due to resorption. The resulting U–Pb analyses also fall into three groups (Fig. 3a, Table 2). Group (i), coinciding with the large grains of morphology group (a), constitutes low error, concordant to near concordant U–Pb analyses giving ca. 500–480 Ma (Fig. 3b). Of these, the most precise and concordant U–Pb analyses (Mnz2, 3, 21, 25) yield an age range from 498 to 494 Ma. Mnz1 and 5 are discordant (Fig. 3b) with a $^{207}Pb/^{206}Pb$ age of 529 ± 8 and 522 ± 7 Ma, respectively; these indicate inheritance of an older, pre-500 Ma component within these grains. In contrast, the small grains of group (ii), coinciding with morphology (b) and some with (c), yield concordant and discordant U–Pb analyses (some with very large errors) that plot in the U–Pb concordia diagram around 450–420 Ma (Fig. 3a). Mnz16–18 of group (iii) and morphology (c) represent discordant high error analyses with young U–Pb ages (Fig. 3a). The radiogenic Pb contents and $^{206}Pb/^{204}Pb$ ratios are fairly low; however, U concentrations are generally high (576–2,080 ppm).

The results of the ID-TIMS analyses of monazite from the remaining part of the TCU are plotted in Fig. 4. These exhibit a general trend of overlapping $^{206}Pb/^{238}U$ ages, but a range of $^{207}Pb/^{235}U$ ages (e.g. Table 2). Monazite of sample *HT-B10* from the *garnet zone* occurs in grain sizes rarely larger than 64 μm. The subhedral, oval to round, tabular grains have an yellow colour with black or colourless inclusions. Larger grains are clouded, whereas smaller sizes (≤ 40 μm) are dominantly round and clear. The concordant monazite fraction yields an U–Pb age of 384 Ma (Mnz3, Table 2), whereas the other error ellipses of this sample lie, with variable horizontal distance from the ca. 385 Ma point, to the right of the concordia (Fig. 4). Monazite of Grt-St micaschist *HT-B5* from the *staurolite zone* is of oval, round, or euhedral shape, very clear, with some inclusions, and typically small (≤ 40 μm). Due to small size, low concentrations of U, and thus of radiogenic Pb, only one of many monazite analyses yielded a reasonably precise result. The error ellipse of this analysis is also positioned to the right of the concordia, with a $^{206}Pb/^{238}U$ age of 386 Ma. Sparse monazite in heavy mineral separate of *HT-B4-1* occurs as small, clear, pale yellow grains or fragments (< 100 μm) of round to irregular tabular habit. Due to low concentrations of radiogenic Pb, only two of the analysed grains or fractions yielded usable results (Table 2); here, the $^{206}Pb/^{238}U$ ratios (with the lowest uncertainties) are reproducible with an age of ca. 382 Ma. Monazite is also very sparse in high-grade metagreywacke *HT-Bez9* from the *kyanite zone*, with U concentrations so low that only one grain could be successfully analysed by TIMS. The analysis yielded a $^{206}Pb/^{238}U$ age of 382 Ma and shows a reverse discordant error ellipse located above concordia (Fig. 4). In summary, two of the analysed monazite

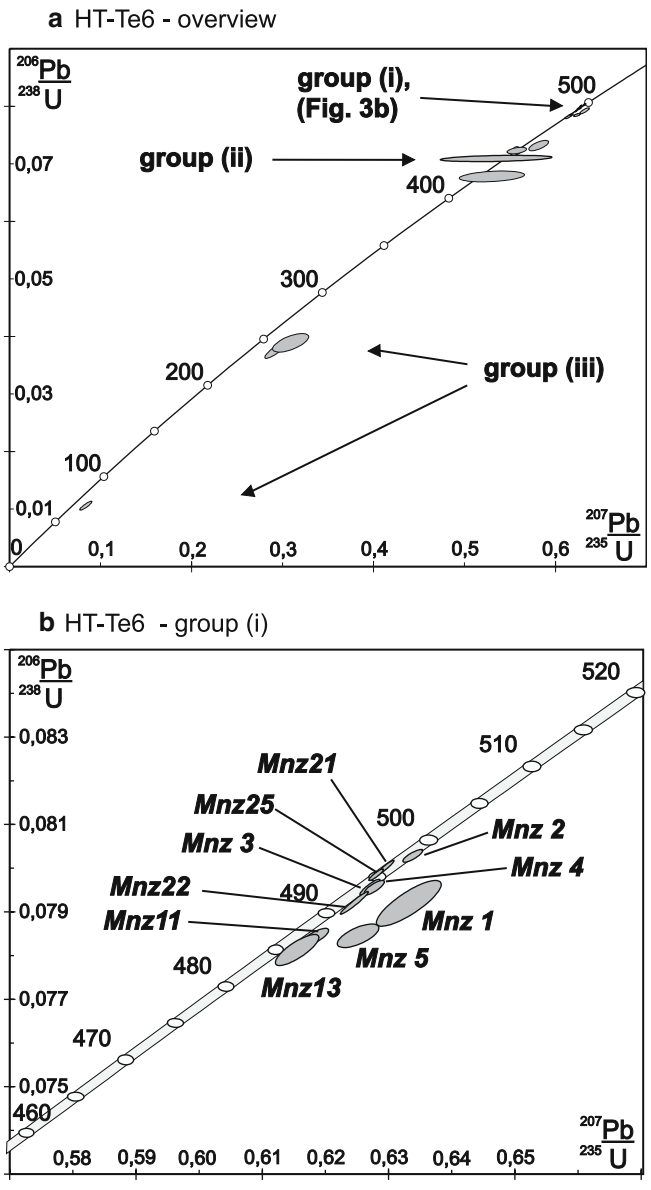

Fig. 3 U–Pb concordia diagrams for migmatitic paragneiss HT-Te6, TCU. **a** Overview of all ID-TIMS monazite analyses, including high error analyses of small monazite [20–40 μm; group (ii)], plotting to the right of the concordia around 450 Ma, and showing some disturbance with respect to their U–Pb systematics, and.monazite of group (iii) showing a very young disturbance. **b** Enlargement of most precise and concordant monazite analyses [group (i)]; these are derived from the largest analysed monazite grains (100 to >250 μm)

fractions are concordant at ca. 385 Ma, whereas the other analyses are slightly (reverse) discordant. Note, however, that the mean $^{206}Pb/^{238}U$ age calculated for all of the analyses shown in Fig. 4 is 385 ± 2 Ma.

Metagabbros: MLC

We carried out additional U–Pb TIMS analyses on zircon from the metagabbro suite at the northwestern boundary of the TCU with the MLC. As these metagabbros are located in direct vicinity to the analysed samples from the TCU, the aim was to determine their emplacement age and find out if the intrusion of the gabbros had an effect on the adjacent paragneisses.

Sample *HT-99-7*, located in a metagabbro train within the northwestern kyanite zone of the TCU (Fig. 2), contains a variety of zircon types, such as longprismatic prisms, shortprismatic, tabular, oval to round, or multifaceted grains or fragments. Zircon 2066, a tabular grain (~180×300 μm) with a clear core, overlaps the concordia with an age of ca. 496 Ma. In contrast, Zircon 2349 and multigrain fractions 2351 and 2353 are variably discordant and plot slightly below the concordia (Fig. 5). Zircon-rich metagabbro *HT-99-8* from the MLC (Fig. 2) contains not only a variety of zircon habits, including longprismatic, clear to internally zoned prismatic grains, but also shortprismatic, isometric to oval, round, and even tabular grains. Several grains are fragmented, and some show resorption. Both multifaceted grains and idiomorphic bipyramidal prisms are rare. The error ellipses of the analysed, mostly concordant, single and multigrain fractions of this sample cluster at or near concordia at ca. 500 Ma (Fig. 5). The most precise age of 503 Ma (Table 2) is given by concordant multigrain fraction 2346. The resulting U–Pb ages from these two metagabbros are taken to reflect an emplacement age for this gabbro suite in the interval from 503 to 496 Ma. Furthermore, the position of the discordant error ellipses of sample HT-99-7 could be due to Pb loss after the ca. 500 Ma emplacement.

EMPA: paragneisses TCU

The chemical composition of monazite of all analysed samples is relatively similar, with low to moderate Th contents (2.5–6 wt% ThO_2), but relatively high U contents (0.5–1.6 wt% UO_2), with the highest values of both occurring in monazite of HT-Te6 (Table 3). The La/Nd ratios range from 0.9 to 1.1, thus indicating a flat LREE pattern. The Y content varies greatly from as low as 0.17 wt% Y_2O_3 in some monazite of the garnet zone (HT-B10) to ca. 2 wt% in monazite from the staurolite zone (HT-B4-1, HT-Kr2-1a), >2 wt% in the kyanite zone (HT-Bez9), and the highest values up to 2.5 wt% in migmatitic paragneiss HT-Te6 (Fig. 6a). Only samples HT-Te6, HT-B4-1, and HT-Kr2-1 show an approximate positive correlation of Y and U concentrations, whereas in HT-B10 and HT-Kr6 these elements appear to be negatively correlated (oxide wt%; see Table 3). Figure 6b demonstrates that in our samples, with few exceptions (e.g. HT-Bez9), there is no unambiguous correlation of Y_2O_3 content and age. Darker and brighter zones within some of the analysed monazite were detected by backscatter electron (BSE) imaging; these are due to contrasting atomic numbers of the elements within these zones, i.e. higher numbers such as Th and U reflect more brightly compared to Y.

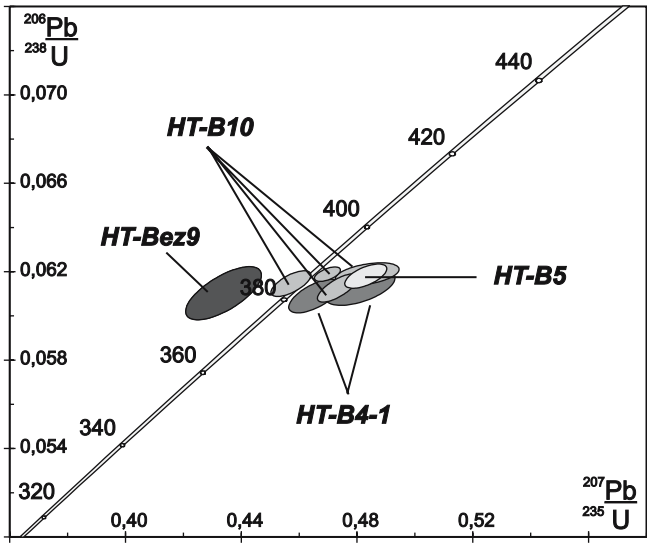

Fig. 4 U–Pb concordia diagram showing ID-TIMS monazite analyses from paragneiss HT-B10, Grt-St micaschist HT-B5, metapelite HT-B4-1, and metagreywacke HT-Bez9, all TCU. For discussion see text

Analysed monazite of samples from the *garnet zone* give a weighted average age of 373 ± 29 Ma for HT-B10, overlapping with the TIMS age of ca. 384 and 375 ± 13 Ma for HT-Kr6. With the exception of a dark zone in HT-B10 (m3B; Table 3), the in situ EMP analyses do not give significantly different ages between the different zones in monazite of both samples.

Monazite ages in the *staurolite zone* are slightly more varied. Distinctly zoned monazite in Grt-St micaschist Bez12 gives older ages around 490 Ma for bright core zones, whereas darker rim areas yield early Variscan ages of ca. 400 Ma (Table 3). Monazite from two different sections of sample HT-Kr2 yield apparent different ages although grain sizes, crystal habits, and the position with respect to the matrix minerals are similar in both. Unzoned monazite of HT-Kr2-1a gives a weighted average age of 376 ± 39 Ma. In contrast, monazite of section HT-Kr2-1 has "old" and "young" domains (though decoupled from core/rim position), despite being unzoned in BSE images. The mean age for the "old" domains is 454 ± 23 Ma and should be taken with care as some of these analyses, such as m3, reflect very low Th and U concentrations. In this case, EMPA are less precise due to the proportionally larger background correction. The mean age for the "young" domains of 393 ± 45 Ma is similar to the Variscan age of previous samples. EMPA of monazite from micaschist HT-B5, derived from the same heavy mineral separate as those analysed by TIMS, give a weighted average age of 373 ± 22 Ma, in support of the more precise $^{206}Pb/^{238}U$ TIMS age of 386 Ma of this sample. Core and rim analyses of monazite from micaschist HT-B4-1 yield the same age within error, which is in agreement with the absence of visible zoning in BSE images. The weighted average age of 382 ± 17 Ma overlaps with the ca. 382 Ma $^{206}Pb/^{238}U$ TIMS age.

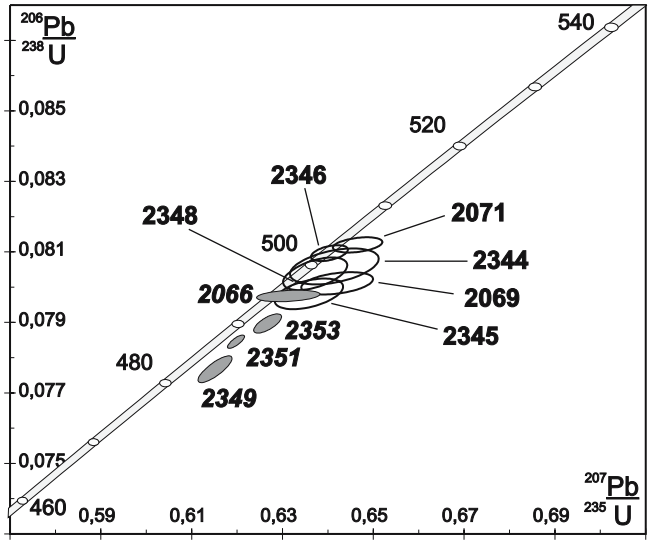

Fig. 5 U–Pb concordia diagram showing ID-TIMS zircon analyses for metagabbros HT-99-7 (*filled ellipses*) and HT-99-8 (*open ellipses*). *Numbers* denote zircon analyses as found in Table 2. For discussion see text

Although backscatter images do not reveal any distinct zoning, some monazite of sample HT-Bez9 from the *kyanite zone* gives older core ages, such as 444 ± 28 Ma in monazite m3. The weighted average age of the remaining younger analyses gives 373 ± 25 Ma. We also note that in this sample, the oldest monazite grain (m3) also has the highest Y concentration (Table 3). EMPA monazite ages of migmatitic paragneiss HT-Te6 vary strongly, most common are ages around 530, 480, 450 and 380 Ma (Table 3). The older ages are typically associated with bright zones in BSE image, whereas younger ages are restricted to the darker domains within the monazite grains. Monazite 5 in BSE image (Fig. 7a) shows no distinct zoning. The two main analyses (done with a broad, defocused beam) are characterised by two bright spots in the upper half of the grain. These yield distinctly different ages; the centre spot gives 537 ± 26 Ma and the rim spot 380 ± 26 Ma. In addition to the main analyses, shorter ones (with a focussed beam) were done along two profiles. Profile 1 (Fig. 7a, white stars) gives altogether older ages with ca. 540 Ma in the grain centre and ages as low as 470 Ma towards the rim. Profile 2 (Fig. 7a, black stars) exhibits older ages of 540–520 Ma in the bright core area, and younger ones—as young as 451 Ma—at the darker rim. In contrast, BSE image of monazite 9 shows quite distinct zoning, a bright centre and a darker rim, but the two main analyses give rather similar ages with an error of 462 and 446 Ma. The ages from the EMPA profile (Fig. 7b, white stars), however, proves that the bright centre zone hosts older monazite (531 Ma) compared to the slightly darker outer zones of this grain (406 Ma). The ages within the transitional zones mostly lie around 480–460 Ma and appear to be mixtures. The size of grains 5 and 9 is similar to those of the small monazite

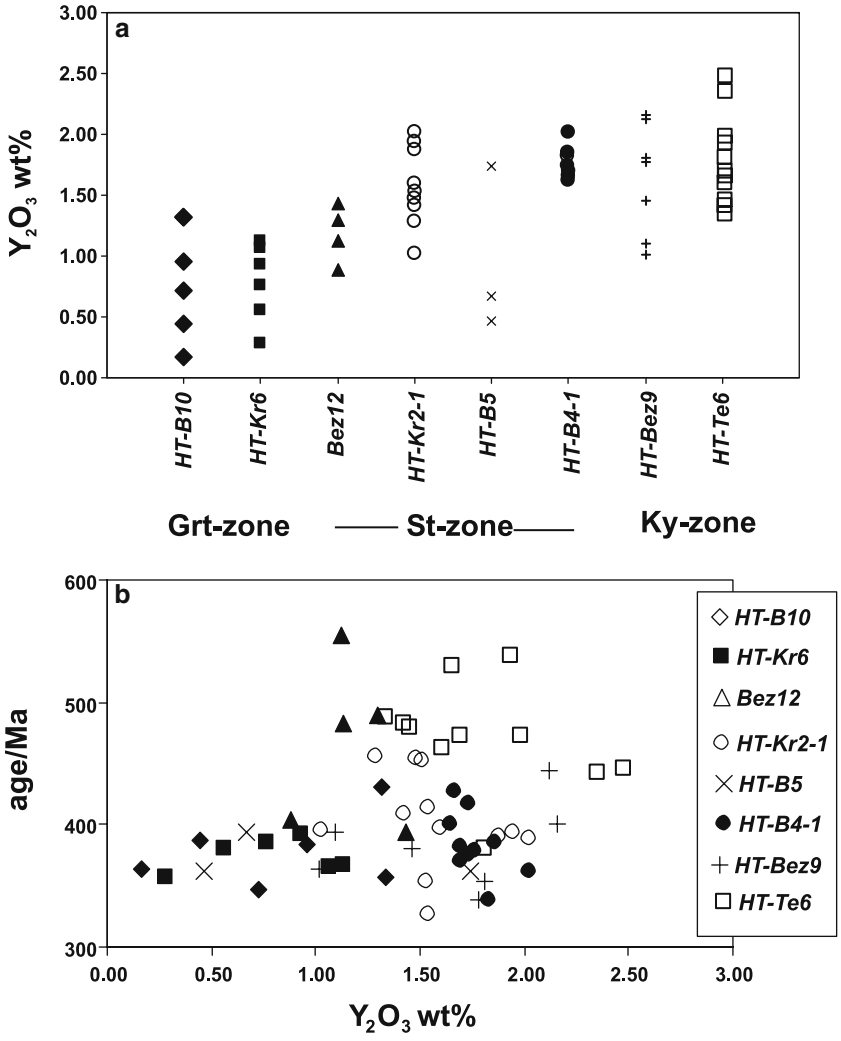

Fig. 6 **a** Y concentrations as Y_2O_3 wt% of monazite from paragneisses of the TCU determined by EMPA. Monazite of each sample has variable Y concentrations, but the maximum Y content in each sample does increase with progressing metamorphic grade. **b** EMPA ages versus Y_2O_3 wt% of analysed monazite. Note that in higher grade samples (e.g. HT-Bez9), the Y content correlates with age

grains analysed by TIMS; these showed disturbance and plot near concordia around 450 Ma [group (ii), Fig. 3a].

Discussion and synthesis

Interpretation of geochronological data

Comparative U–(Th–)Pb analyses by ID-TIMS and chemical EMPA dating were done on monazite in paragneisses from the TCU, with additional zircon analyses from two metagabbro samples of the MLC.

Concordant ID-TIMS analyses of monazite from migmatitic paragneiss HT-Te6 in the northwesternmost TCU imply monazite growth at 498–494 Ma. This growth phase does not overlap with the timing of either Variscan or the earlier Cadomian metamorphism. Monazite grains in HT-Te6 that are smaller than 100 µm, however, are discordant or indicate a major, young overprint. Furthermore, pre-500 Ma monazite components were detected by ID-TIMS analyses in HT-Te6 (Mnz1, Mnz5). Backscatter imaging and EMPA reveal the very inhomogeneous nature of monazite from HT-Te6, showing a mix of various age domains from ca. 540 to 380 Ma.

Isotope dilution–thermal ionisation mass spectrometry analyses of monazite from the remaining part of the TCU were hampered by its low abundance within those rocks, its small size, and its variable common Pb content. The few monazite grains analysed have similar $^{206}Pb/^{238}U$ ages, but show a range of $^{207}Pb/^{235}U$ ages. Sample HT-Bez9 yielded only one, reverse discordant analysis. Although reverse discordance can be caused by analytical problems, it is common in monazite when Th/U ratios are high. Monazite incorporates high amounts of Th, generally ^{232}Th, but also ^{230}Th which is unstable and decays to ^{206}Pb. This "excess" ^{206}Pb increases the ratio of $^{206}Pb/^{238}U$, and thus results in error ellipses that are located above the concordia (e.g. Schärer 1984; Parrish 1990). Here, however, reverse discordance of TIMS analyses was detected in only this one monazite analysis of sample HT-Bez9. Furthermore, the Th/U ratio of this monazite is 4.14, which is (a) not very high and (b) exactly comparable to the Th/U ratios of the other, "normal" discordant analyses (Table 2). Excess ^{206}Pb therefore does not seem to be the major cause for

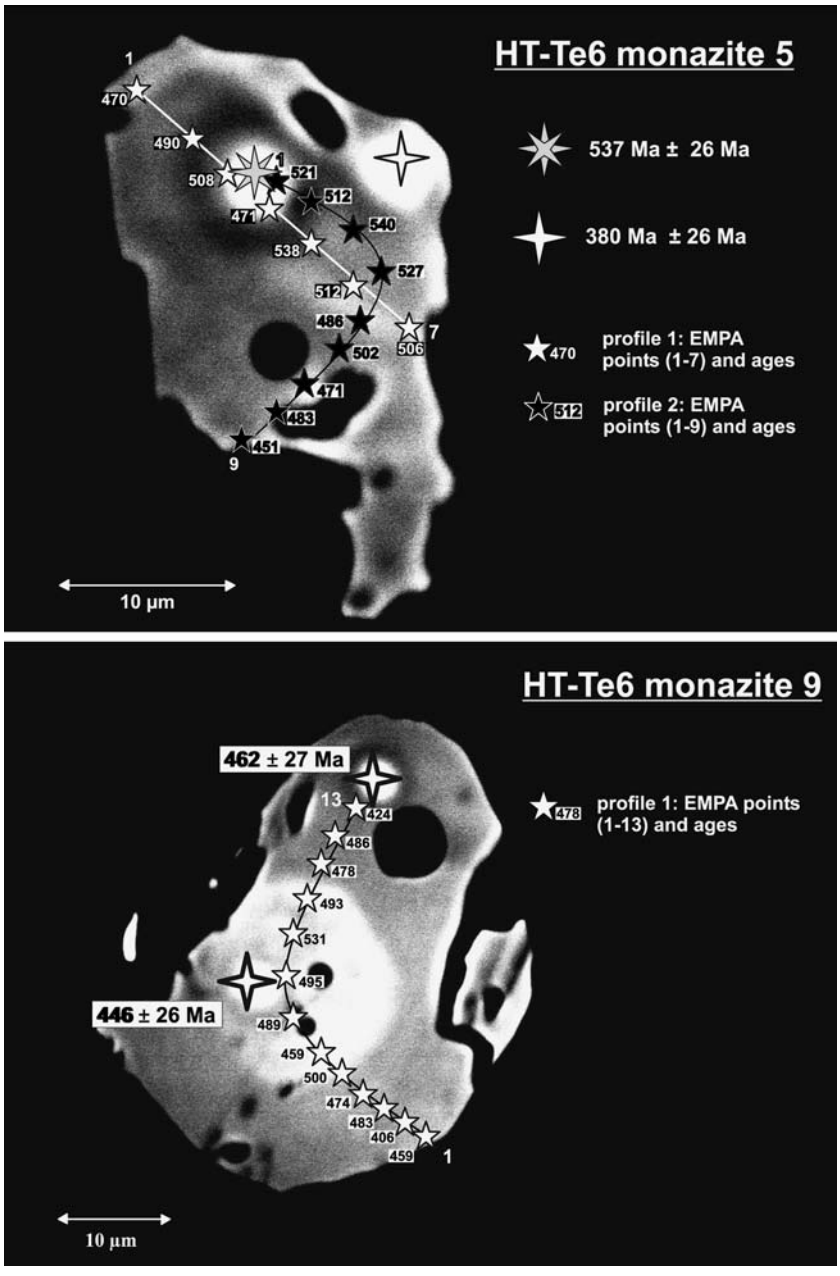

Fig. 7 BSE images of monazite from HT-Te6. **a** The two main EMPA analyses (*bright spots*) of unzoned monazite 5 yield ages of 537 ± 26 and 380 ± 26 Ma for core and rim, respectively. Profile 1 includes seven analyses (*white stars*), profile 2 nine analyses (*black stars*), with older EMPA ages in the core area, younger ones at the rim, and transitional ages in between. **b** Main EMPA spots in monazite 9 give similar ages of 462 ± 27 and 446 ± 26 Ma. Profile 1 (*white stars*) shows that bright centre zone yields older monazite ages and younger ones in the slightly darker outer zones of this grain

the range of $^{207}Pb/^{235}U$ ages. The monazite of HT-Bez9, however, does have the highest common Pb content (5.2%), compared to the analyses of monazite in HT-B10, HT-B5, and HT-B4-1. When subtracting common Pb (amount of Pb incorporated into the crystal structure at the time of crystallisation) from the analysis, the correct initial Pb isotopic composition has a significant effect on the position of the error ellipses with respect to the concordia. If, as is the case here, a sample is small and the proportion of initial common Pb in comparison to radiogenic Pb high, the ellipses may be shifted, here slightly to the left. However, monazite of samples HT-B10, HT-B5, and HT-B4-1 has lower common Pb contents and still gives error ellipses positioned slightly beside the concordia due to a (slight) variation of $^{207}Pb/^{235}U$ ages. An erroneous common Pb correction cannot thus be the cause for the range of $^{207}Pb/^{235}U$ ages either, at least not for these three samples. We rather note the general little amounts of radiogenic Pb within monazite of these samples, with ^{207}Pb making up the smallest proportion and thus the smallest signal to analyse, which therefore is associated with larger errors compared to the higher signals for the ^{206}Pb and ^{208}Pb isotopes. For sample HT-Te6, however, the high analytical errors of monazite of group (ii) are due to a combination of both low radiogenic Pb contents *and* high amounts of common Pb (4–35%), especially in the small grains. Instead of Pb incorporation into monazite at the time of initial crystallisation common Pb may also have migrated into the crystal later (e.g. Mathieu et al.

2001). Pb mobilisation may occur during thermal events, latter of which also causes dissolution and alteration of monazite (see below). The resulting porous crystal structure of monazite then allows incorporation of migrated external Pb (Mathieu et al. 2001). Small grains have a greater surface/volume ratio in comparison to large grains, which could facilitate migration of relatively higher concentrations of Pb into the crystal; this may explain our observation of small monazite [group (ii) in Fig. 3a] containing the proportionally largest amounts of common Pb.

For our interpretation of samples HT-B5, HT-B4-1, HT-B10, and HT-Bez9, we use the $^{206}Pb/^{238}U$ ages as these are based on higher signals and thus lower errors compared to the $^{207}Pb/^{235}U$ ages. The $^{206}Pb/^{238}U$ TIMS ages define a narrow range from 387 to 382 Ma. In comparison, the EMPA monazite ages from the paragneisses of the northern Grt- and St-zones give a slightly lower but still overlapping range of U–Pb ages from 382 to 373 Ma. Note that the location of monazite within the grain mount or polished section is irrelevant for the age distribution. We interpret both TIMS and EMPA monazite ages to reflect the Variscan regional metamorphism in this area. Exceptions are EMPA from polished sections of the central TCU (HT-Kr2-1, Bez12, HT-Bez9) that yield a range of ages, ca. 480, 450 and 390 Ma. These indicate inheritance of older components within individual grains and imply that some monazite grew in pre-Variscan times. Bearing in mind the mixing of age domains from ca. 540 to 380 Ma in sample HT-Te6, the ca. 480 and 450 Ma EMPA ages from the central TCU may reflect mixtures of pre-Variscan and Variscan age domains. However, the common occurrence especially of the 490–480 Ma ages would imply frequent mixing of the same proportions. Instead, the ca. 480 Ma EMPA ages all overlap within error with the concordant 498–494 Ma TIMS ages, and we interpret these as real ages.

The zircon analyses from the metagabbros in the boundary zone between the MLC and the TCU yielded concordant ages from 503 to 496 Ma that are interpreted to date their emplacement in mid- to lower crustal levels. These data are supported by a 496 Ma age for gabbro pegmatite crystallisation from Bowes and Aftalion (1991) and coincide with the age of concordant monazite in paragneiss HT-Te6 in the northwesternmost TCU. We therefore conclude that the 498–494 Ma monazite from the migmatitic paragneiss grew as a direct result of the ca. 500 Ma metagabbro intrusion, and not as a response to either the Cadomian or the later Variscan regional metamorphism.

Implications for the processes involving monazite formation

This study shows that, especially in the more northern areas of the TCU, pre-Variscan monazite coexists next to younger monazite. Furthermore, pre-500 Ma monazite components in HT-Te6 indicate a major overprint leading to the existence of ca. 500-Ma-old monazite. The process responsible for this could be either Pb loss by volume diffusion, recrystallisation, or dissolution and reprecipitation. During Variscan regional metamorphism, peak temperatures in the staurolite zone reached ≥500°C, whereas *P–T* conditions in the garnet zone were around 500°C and 5–6 kbar (Zulauf 1997a). However, coefficients for Pb diffusion in monazites are very low, and estimated closure temperatures of at least 700–750°C (see above) are much higher than those experienced by the rocks of the TCU during the Variscan metamorphism. Thus, the ''reset'' U– Th–Pb systematics in monazite of both the St- and the Grt-zones, at least in the northern part and in small monazites (≤ 100 μm), cannot be the result of Pb loss by volume diffusion. Small monazite grains in HT-Te6 close to the MLC are discordant, the disturbed U–Th–Pb systematics being due to a mixing of different age domains as shown with backscatter imaging. The different age domains are also characterised by distinct zoning. The brighter domains, mainly located in the grain centre, have higher Th and U and lower Y contents, whereas the rims are typically darker and Th poorer. The chemical composition of monazite is typical for paragneisses (e.g. Finger and Helmy 1998). The Y contents of monazite within the individual samples are quite varied, which points to the fact that there is no Y saturation in any of the analysed samples, and is in agreement with the absence of xenotime. However, we have shown in Fig. 6a that the maximum Y content in the samples does increase with progressing metamorphic grade. This corresponds to Heinrich et al.'s (1997) demonstration of a positive correlation of Y content with metamorphic grade. Apart from xenotime, garnet also strongly controls the Y/HREE content in coexisting monazite (e.g. Pyle et al. 2001; and references therein). As the dominant garnet in the kyanite zone is GrtII of the second, Variscan generation (Záček 1994), the occurrence of the highest Y concentrations within the pre-Variscan monazite of sample HT-Te6 corresponds to their occurrence in a garnet-free assemblage. Furthermore, the two oldest grains in HT-Bez9 of the kyanite zone have the highest Y concentrations, which may point to the fact that they would have originated within the garnet-free Cadomian mineral assemblage. Instead Variscan monazite in HT-Bez9 grew together with garnet II and are correspondingly Y poorer. Widespread garnet growth during the Variscan may in fact play a major role for major monazite ''resetting'' at ca. 380 Ma. As demonstrated by Pyle and Spear (2000), in the absence of xenotime during prograde metamorphism, monazite will be consumed during garnet growth, which in our case would be the pre-380 Ma monazite, and with progressing metamorphism (post-St-isograde) new low-Y monazite grows together with garnet.

Looking at the earlier phase of monazite (re-)growth at ca. 500 Ma, we must bear in mind that Cadomian regional metamorphism was long over, whereas the

numerous granitoid and metagabbro intrusions rather point to widespread tectonomagmatic activity at that time. This led to a high fluid activity in the crust at this time, a condition that lasted from ca. 500 Ma until at least 487–475 ± 5 Ma and is reflected by the widespread pegmatite intrusions in the TCU. By comparison with both experimental and field studies concerned with formation of monazite, we therefore believe that hydrothermal dissolution and reprecipitation is a more likely process for an alteration of the original pre-500 Ma signature in monazite of sample HT-Te6. Zeh et al. (2003) similarly found that monazite in paragneisses of the Ruhla crystalline complex in central Germany grew or recrystallised contemporaneous with the emplacement of voluminous diorite and granite bodies in the Lower Carboniferous.

Teufel and Heinrich (1997) experimentally determined the importance of hydrothermal influence on the U–Pb isotope system in monazite. For their study they used a monazite from a lower amphibolite facies metapelite of the Zone of Erbendorf-Vohenstrauss (ZEV) from NE Bavaria in Germany. Hydrothermal treatment caused dissolution of ground monazite and reprecipitation, with Pb concentrations decreasing, and U–Pb ages younging, with increasing temperature. Teufel and Heinrich (1997) proposed that this mechanism may be responsible for resetting of the U–Th–Pb systematics in monazite at temperatures as low as 400°C; these were reached in both the Grt- and St-zones of the TCU. Furthermore, Seydoux-Guillaume et al. (2002) showed with an experimental study the efficiency of dissolution and reprecipitation as mechanism for controlling the ''resetting'' of monazite in natural rocks. These authors demonstrated that the extent of dissolution and reprecipitation of hydrothermally treated monazite depends on the fluid composition. The experimental results are supported by several field-based studies of hydrothermally overprinted monazite (e.g. Townsend et al. 2000; Rasmussen et al. 2001; Rasmussen and Fletcher 2002). Interestingly, Krohe and Wawrzenitz (2000) point to the importance of stress as inducing dissolution and precipitation of monazite. In a study of monazite ages from polymetamorphic paragneisses from the KTB drilling site they found differing monazite ages in domains that had experienced varying deformation mechanisms. Monazites that underwent diffusion creep (i.e. dissolution and reprecipitation) were discordant, whereas no resetting took place by volume diffusion in Mid-Devonian paragneisses that had experienced temperatures above 650°C. In comparison to our study, however, the change of the deformation regime at the St-isograde (from localised D3 deformation and F3 folding in the greenschist facies domain to pervasive mylonitic D3 shearing in the amphibolite facies domain; Zulauf 2001) does not correlate with the distribution pattern of less and complete resetting of older monazite.

The Pb-poorer, discordant, young monazites [group (iii)] in HT-Te6 remind of monazite decomposition and rhabdophane formation during alpine, fluid-dominated very low grade metamorphism in Crete (Finger et al. 2002; Krenn and Finger 2002). These authors observed decomposition of monazite at conditions of 300°C and 6 kbar by dissolution in a Cl and F-bearing fluid and reprecipitation as low-Y monazite, allanite, or rhabdophane ($LREEPO_4 \cdot H_2O$). During the process of dissolution and reprecipitation, Pb remains in the fluid phase, so that the newly grown monazites are generally Pb poorer (Teufel and Heinrich 1997). This may also explain the lower Pb content in the smaller, most disturbed fractions of HT-Te6 [group (iii) in Fig. 3a, Table 2].

The evidence provided here points to the fact that monazite growth or regrowth must have happened by a different process than Pb loss by volume diffusion, and the term ''resetting'' cannot be applied to these monazites anymore. Instead, recrystallisation and dissolution/reprecipitation seem to be more probable mechanisms. More detailed information on fluid compositions, however, require further microchemical investigations.

Tectonic evolution

The Cadomian regional event is manifested in the TCU by the intrusion of Cambrian granitoids into deformed and metamorphosed upper Proterozoic sediments (Dörr et al. 1998), as well as by discordant monazite TIMS data from sample HT-Te6 in the vicinity of the MLC. In the southern part of the TBU, EMPA ages of monazites from the DCC around ca. 540 Ma were interpreted to reflect the peak of Cadomian regional metamorphism, as a result of collision of a microterrane or arc with the TBU at the northern active margin of Gondwana (Zulauf et al. 1999). Subsequent synkinematic intrusion of various plutons at 524–522 Ma into transtensive shear zones of the DCC might be the result of remelting of arc-type crust after postcollisional slab break-off (Zulauf et al. 1997). These plutons are located not only in the DCC, but also in the southerly, mafic Neuenkirchen Kdyně massif (Dörr et al. 2002). Instead, those of the TCU are interpreted to belong to a different magmatic period, latter represented by the ≤ 500 Ma emplacement of a suite of metagabbros into the boundary zone of the TCU and MLC. The granitoids of the TCU were dated by Dörr et al. (1998) from 516 to 511 Ma; however, these ages are based on upper intercepts of mainly slightly discordant analyses. Concordant to nearly concordant ages of the Lestkov metagranitoid and the Hanov orthogneiss, however, rather indicate intrusion around 500 Ma. Furthermore, on the base of field relationships Štědrá et al. (2002) proposes that intrusion of metagabbros and granitoids of the TCU was coeval. The ca. 500-Ma-old metagabbros generally reflect within-plate basalt or oceanic island geochemistries and are generally interpreted to be the first evidence of the rifting event at the northern margin of Gondwana that led to the separation of Armorica. Similarly, the granitoids of volcanic-arc

affinities are taken to reflect a transtensional setting associated with the beginning break-up of the northern active Gondwana margin (Dörr et al. 1998). Thereby, the granitoids do not reflect a juvenile arc, but instead remelting of pre-existing arc-type crust, by high thermal input from slab break-off after culmination of late Cadomian subduction (Zulauf et al. 1999). This implies not only advective thermal input into the different levels of the crust through the melts and associated rheological weakening, but also a high fluid activity at this time. The high fluid activity would have caused (nearly complete) dissolution of older monazite in the paragneisses and reprecipitation of new monazite, especially in the direct vicinity of the heat/fluid suppliers; this is manifested in sample HT-Te6. Most importantly, however, monazite growth at ca. 500 Ma in response to the vicinity of metagabbro intrusion in the TCU–MLC boundary proves that both units must have been associated already at this time.

As part of this same major plutonic event, but at a later stage, happened the emplacement and crystallisation of numerous pegmatites at 487–475 ± 5 Ma (Glodny et al. 1998), further aiding fluid-activated dissolution and reprecipitation of monazite. Similar processes operated at the same time not only in the DCC (H. Timmermann et al., in preparation), but also in the Neuenkirchen Kdyně massif, as indicated by K–Ar ages reflecting resetting in biotite at 518–491 and 495 Ma within the two northern plutons (Bues et al. 2002). The distribution of the ca. 500–480 Ma age is more widespread still, as evidenced by geochronological data from other tectonic units in Central Europe. Protolith crystallisation of metagabbros with relict ophitic structures of the ZEV was dated at 496–476 Ma (von Quadt 1997). Similarly, replotting the U–Pb analyses of Gebauer and Grünenfelder (1979) using Isoplot (Ludwig 2001) yields concordant zircon ages of 496 ± 3 Ma for metagabbro emplacement in the Münchberg Massif (MM). Furthermore, zircon overgrowths in paragneisses of the ZEV were SHRIMP dated at 487 ± 13 Ma (Söllner and Nelson 1995), Rb–Sr ages from igneous muscovites of metapegmatites give ages of 481–473 ± 5 Ma (Glodny et al. 1998), and Krohe and Wawrzenitz (2000) report U–Pb monazite ages from polymetamorphic paragneisses from the ZEV of ~484 Ma, basically the same age range as in the TCU. This implies igneous activity and associated major fluid presence in the crust in the Cambro-Ordovician and further strengthens previous arguments for a similar geological history of the TCU, MLC, MM, and ZEV (e.g. Dörr et al. 2002; Timmermann et al. 2004).

Major new monazite growth at ca. 380 Ma in the TCU is ascribed to Variscan regional metamorphism, caused by the collision of the TBU with the Saxothuringian unit (e.g. Franke 1989; Matte et al. 1990). This was followed by fast exhumation and cooling, as evidenced by the postpeak metamorphic ages from the TBU: Rb–Sr ages around 375 Ma (Glodny et al. 1998) and Ar–Ar data ranging from ca. 380 to 350 Ma (Dallmeyer and Urban 1994; Zulauf 1997a). Thus, the results of this study provide the first U–Th–Pb ages for the peak of Variscan metamorphism in this area.

Acknowledgements This research was supported by DFG project Do 572/1-1. We thank Bernd Herrmann and Martin Wehnisch for mineral separation and J. Schastok for laboratory assistance. We further thank J. Glodny and I. Broska for the valuable comments that helped to improve the manuscript.

References

Beard BL, Medaris LG, Johnson CM, Jelínek E, Tonika J, Riciputi LR (1995) Geochronology and geochemistry of eclogites from the Mariánské Lázně complex, Czech republic: implications for Variscan orogenesis. Geol Rundsch 84:552–567

Bowes DR, Aftalion M (1991) U–Pb zircon isotope evidence of Early Ordovician and Late Proterozoic units in the Mariánské Lázně Complex, Central European Hercynides. N Jb Mineral Mh 7:315–326

Bues C, Dörr W, Fiala J, Vejnar Z, Zulauf G (2002) Emplacement depth and radiometric ages of Paleozoic plutons of the Neukirchen-Kdyně massif: differential uplift and exhumation of Cadomian basement due to Carboniferous orogenic collapse (Bohemian Massif). Tectonophysics 352:225–243

Cháb J, Záček V (1994) Metamorphism of the Teplá Crystalline complex. KTB Rep 94(3):33–37

Cháb J, Suchý, Vejnar Z (1995) Metamorphic evolution. In: Dallmeyer RD, Franke W, Weber K (eds) Pre-permian geology of Central and Eastern Europe. Springer, Berlin Heidelberg New York, pp 404–410

Cháb J, Šrámek J, Pokorný L, Chlupáčová M, Manová M, Vejnar Z, Waldhauserová J, Žáček V (1997) The Teplá-Barrandian unit. In: Vrana S, Štědrá V (eds) Geological model of western Bohemia related to the KTB borehole in Germany. J Geol Sci CGS Prague 47, pp 80–104

Chaloupský J, Chlupáč I, Mašek J, Waldhausrová J, Cháb J (1995) Teplá-Barrandian Zone (Bohemicum) stratigraphy. In: Dallmeyer RD, Franke W, Weber K (eds) Pre-permian geology of Central and Eastern Europe. Springer, Berlin Heidelberg New York, pp 379–391

Cherniak DJ, Watson EB, Grove M, Harrison, TM (2004) Pb diffusion in monazite: a combined RBS/SIMS study. Geochim Cosmochim Acta 68:829–840

Chlupáč I (1993) Geology of the Barrandian. A field trip guide. Waldemar-Kramer, Frankfurt a M, 163 pp

Cocherie A, Legendre O, Peucat JJ, Kouamelan AN (1998) Geochronology of polygenetic monazites constrained by in-situ electron microprobe Th–U total lead determination: implications for lead behaviour in monazite. Geochim Cosmochim Acta 62:2475–2497

Copeland P, Parrish RR, Harrison TM (1988) Identification of inherited Pb in monazite and ist implications for U–Pb systematics. Nature 333:760–763

Crowley JL, Ghent ED (1999) An electron microprobe study of the U–Th–Pb systematics of metamorphosed monazite: the role of Pb diffusion versus overgrowth and recrystallisation. Chem Geol 157:285–302

Dallmeyer RD, Urban M (1994) Variscan vs Cadomian tectonothermal evolution within the Teplá-Barrandian zone, Bohemian Massif, Czech Republic: $^{40}Ar/^{39}Ar$ mineral and whole-rock slate/phyllite ages. J Czech Geol Soc 39:21–22

De Wolf CP, Belshaw NS, O'Nions R, Keith A (1993) Metamorphic history from micron-scale $^{207}Pb/^{206}Pb$ chronometry of Archean monazite. Earth Planet Sci Lett 120:207–220

Dodson MH (1973) Closure temperature in cooling geochronological and petrological systems. Contrib Mineral Petrol 40:259–274

Dörr W, Fiala J, Vejnar Z, Zulauf G (1998) U–Pb zircon ages and structural development of metagranitoids of the Teplá crystalline complex: evidence for pervasive Cambrian plutonism within the Bohemian massif (Czech Republic). Geol Rundsch 97:135–149

Dörr W, Zulauf G, Fiala J, Franke W, Vejnar Z (2002) Neoproterozoic to Early Cambrian history of an active plate margin in the Teplá Barrandian unit—a correlation of U–Pb isotopic-dilution-TIMS ages (Bohemia, Czech Republic). Tectonophysics 352:65–85

Fiala F (1948) Conglomerats algonkins de la Boheme centrale. Sbornik statniho geologickeho Ustavu Ceskoslovenske Republiky 15:399–612

Finger F, Helmy HM (1998) Composition and total-Pb model ages of monazite from high-grade paragneisses in the Abu Swayel area, southern Eastern Desert. Egypt Mineral Petrol 62:269–289

Finger F, Krenn E, Riegler G, Romano S, Zulauf G (2002) Resolving Cambrian, Carboniferous, Permian and Alpine monazite generations in the polymetamorphic basement of eastern Crete (Greece) by means of the electron microprobe. Terra Nova 14:233–240

Foster G, Gibson HD, Parrish RR, Horstwood M, Fraser J, Tindle A (2002) Textural, chemical and isotopic insights into the nature and behaviour of metamorphic monazite. Chem Geol 191:183–207

Franke W (1989) Tectonostratigraphic units in the Variscan belt of central Europe. Geol Soc Am Spec Pap 230:67–90

Gebauer D, Grünenfelder M (1979) U–Pb zircon and Rb–Sr mineral dating of eclogites and their country rocks. Example: Münchberg Gneiss Massif, Northeast Bavaria. Earth Planet Sci Lett 42:35–44

Glodny J, Grauert B, Fiala J, Vejnar Z, Krohe A (1998) Metapegmatites in the western Bohemian massif: ages of crystallisation and metamorphic overprint, as constrained by U–Pb zircon, monazite, garnet, columbite and Rb–Sr muscovite data. Geol Rundsch 87:124–134

Heaman LM, Parrish RR (1991) U–Pb geochronology of accessory minerals. In: Heaman L, Ludden JN (eds) Applications of radiogenic isotope systems to problems in geology. MAC Short Course Handbook 19

Heinrich W, Andrehs G, Franz G (1997) Monazite-xenotime miscibility gap thermometry. I. An empirical calibration. J Met Geol 15:3–16

Jelínek E, Štědrá V, Cháb J (1997) The Mariánské Lázně complex. In: Vrana S, Štědrá V (eds) Geological model of western Bohemia related to the KTB borehole in Germany. J Geol Sci 47

Kastl E, Tonika J (1984) The Mariánské Lázně metaophiolitic complex (west Bohemia). Krystal 17:59–76

Kettner R (1917) Versuch einer stratigraphischen Einteilung des böhmischen Algonkiums. Geol Rundsch 8:169–188

Krenn E, Finger F (2002) Zur Stabilität von Monazit bei der Metamorphose. Erlanger Geol Abh Sonderband 3, TSK9

Kretz R (1983) Symbols for rock-forming minerals. Am Mineral 68:277–279

Krogh TE (1973) A low contamination method for hydrothermal decomposition of zircon and extraction of U and Pb for isotopic age determinations. Geochim Cosmochim Acta 37:485–494

Krogh TE (1982) Improved accuracy of U–Pb ages by the creation of more concordant systems using an air abrasion technique. Geochim Cosmochim Acta 46:637–649

Krohe A, Wawrzenitz N (2000) Domainal variations of U–Pb monazite ages and Rb–Sr whole rock dates in polymetamorphic paragneisses (KTB Drill Core, Germany): influence of strain and deformation mechanisms on isotope systems. J Met Geol 18:271–291

Ludwig KR (1980) Calculation of uncertainties of U–Pb isotope data. Earth Planet Sci Lett 46:212–220

Ludwig KR (2001) User's manual for Isoplot/Ex Version 2 49, A geochronological toolkit for Microsoft Excel. Berkley Geochronology Center Spec Pub 1a, Berkley

Manhès G, Allègre CJ, Dupré B, Hamelin B (1979) Lead–lead systematics, the 'age of the earth' and the chemical evolution of our planet in a new representation space. Earth Planet Sci Lett 44:91–104

Mathieu R, Zetterström L, Cuney M, Gauthier-Lafaye F, Hidaka H (2001) Alteration of monazite and zircon and lead migration as geochemical tracers of fluid paleocirculations around the Oklo-Okélobondo und Bangombé natural nuclear reaction zones (Franceville basin, Gabon). Chem Geol 171:147–171

Matte P, Maluski H, Reilich P, Franke W (1990) Terrane boundaries in the Bohemian Massif: results of large scale Variscan shearing. Tectonophysics 177:151–170

Mašek J (1994) Proterozoic of the Central Bohemian region (Bohemicum). In: Klomínský J (eds) Geological atlas of the Czech Republic: stratigraphy. Czech Geol Surv, Praha, pp 1–1

Montel JM, Foret S, Veschambre M, Nicollet Ch, Provost A (1996) A fast, reliable, inexpensive in-situ dating technique: electron microprobe ages on monazite. Chem Geol 131:37–53

Parrish RR (1987) An improved micro-capsule for zircon dissolution in U–Pb geochronology. Chem Geol 66:99–102

Parrish RR (1990) U–Pb dating of monazite and its application to geological problems. Can J Earth Sci 27:1431–1450

Pyle JM, Spear FS (2000) Accessory-phase paragenesis in low P-migmatites, Chesham pond nappe, SE New Hampshire. Geol Soc Am Ann Meet Abstr 32:A297

Pyle JM, Spear FS, Rudnick RL, McDonough WF (2001) Monazite-xenotime-garnet equilibrium in metapelites and a new monazite-garnet thermometer. J Petrol 42:2083–2107

von Quadt A (1997) U–Pb zircon and Sr–Nd–Pb whole-rock investigations from the continental deep drilling (KTB). Geol Rundsch 86:S258–S271

Rasmussen B, Fletcher IR (2002) Indirect dating of mafic intrusions by SHRIMP U–Pb analysis of monazite in contact metamorphosed shale: an example from the Palaeoproterozoic Capricorn Orogen, Western Australia. Earth Planet Sci Lett 197:287–299

Rasmussen B, Fletcher IR, McNaughton NJ (2001) Dating low-grade metamorphic events by SHRIMP U–Pb analysis of monazite in shales. Geol 29:963–966

Rubatto D, Williams IS, Buick IS (2001) Zircon and monazite response to prograde metamorphism in the Reynolds Range, central Australia. Contrib Mineral Petrol 140:458–468

Schärer U (1984) The effect of initial ^{230}Th disequilibrium on young U–Pb ages: the Makalu case, Himalaya. Earth Planet Sci Lett 67:191–204

Scherrer NC, Engi M, Gnos E, Jakob V, Liechti A (2000) Monazite analysis—from sample preparation to microprobe age dating and REE quantification. Schweiz Mineral Petrol Mit 80:93–105

Seydoux-Guillaume A-M, Paquette J-L, Wiedenbeck M, Montel J-M, Heinrich W (2002) Experimental resetting of the U–Th–Pb systems in monazite. Chem Geol 191:165–181

Smith HA, Giletti BJ (1997) Lead diffusion in monazite. Geochim Cosmochim Acta 61:1047–1055

Söllner F, Nelson D (1995) Polyphase growth history of the gneiss zircons from the continental deep drilling program (KTB): preliminary evidence from U–Th–Pb ion microprobe analyses (SHRIMP). Terra Nova 7:350

Spear FS, Parrish RR (1996) Petrology and cooling rates of the Valhalla Complex, British Columbia, Canada. J Petrol 37:733–765

Stacey JS, Kramers JD (1973) Approximation of terrestrial lead isotope evolution by a two-stage model. Earth Planet Sci Lett 26:207–221

Suzuki K, Adachi M, Tanaka T (1991) Middle Precambrian provenance of Jurassic sandstone in the Mino Terrane, central Japan: Th–U–total Pb evidence from an electron microprobe monazite study. Sed Geol 75:141–147

Suzuki K, Adachi M, Kajizuka I (1994) Electron microprobe observations of Pb diffusion in metamorphosed detrital monazites. Earth Planet Sci Lett 128:391–405

Teufel S, Heinrich W (1997) Partial resetting of the U–Pb isotope system in monazite through hydrothermal experiments: an SEM and U–Pb isotope study. Chem Geol 137:273–281

Timmermann H, Stedra V, Gerdes A, Noble S, Parrish RR, Dörr W (2004) The problem of dating HP metamorphism: an U–Pb isotope and geochemical study on eclogites and related rocks of the Mariánské Lázne Complex, Czech Republic. J Petrol 45:1311–1338

Townsend KJ, Miller CF, D'Andrea JL, Ayers JC, Harrison TM, Coath CD (2000) Low temperature replacement of monazite in the Ireteba granite, Southern Nevada: geochronological implications. Chem Geol 172:95–112

Vavra G, Schaltegger U (1999) Post-granulite facies monazite growth and rejuvenation during Permian to Lower Jurassic thermal and fluid events in the Ivrea Zone (Southern Alps). Contrib Mineral Petrol 134: 405–414

Štědrá V, Kryza R, Kachlík V (2002) Coronitic metagabbros of the Mariánské Lázně Complex and Teplá Crystalline Unit: inferences for the tectonometamorphic evolution of the western margin of the Teplá-Barrandian Unit, Bohemian Massif. In: Winchester JA, Pharaoh TC, Verniers J (eds) Palaeozoic amalgamation of Central Europe. Geological Society of London special publication 201, pp 217–236

Waldhausrová J (1984) Proterozoic volcanic and intrusive rocks of the Jilove Zone in Central Bohemia. Krystal 17:77–97

Waldhausrová J (1997) Geochemistry of volcanites (metavolcanics) in the western part of the TBU Precambrian and their original geotectonic setting. In: Vrana S, Štědrá V (eds) Geological model of western Bohemia related to the KTB borehole in Germany. J Geol Sci 47:85–90

Záček V (1994) Garnets and metamorphic evolution of the Teplá crystalline complex, Western Bohemia. Zentralbl Geol Paläont 1(7/8):847–856

Záček V, Slabý J, Cháb J (1993) The metamorphic evolution of the Teplá Crystalline Unit (In Czech). MS Czech Geol Surv Praha

Zeh A, Williams IS, Brätz H, Millar IL (2003) Different age response of zircon and monazite during the tectono-metamorphic evolution of a high grade paragneiss from the Ruhla Crystalline Complex, central Germany. Contrib Mineral Petrol 145:691–706

Zhu XK, O'Nions RK, Belshaw NS, Gibb AJ (1997) Significance of in-situ SIMS chronometry of zoned monazite from the Lewisian granulites, northwest Scotland. Chem Geol 135:35–53

Zulauf G (1997a) Von der Anchizone bis zur Eklogitfazies: Angekippte Krustenprofile als Folge der cadomischen und variscischen Orogenese im Teplá-Barrandium (Böhmische Masse). Geotekt Forsch 89:1–302

Zulauf G (1997b) Constriction due to subduction: evidence for slab pull in the Mariánské Lázně complex (central European Variscides). Terra Nova 9:232–236

Zulauf G (2001) Structural style, deformation mechanisms and paleodifferential stress along an exposed crustal section: constraints on the rheology of quartzofeldspathic rocks at supra- and infrastructural levels (Bohemian Massif). Tectonophysics 332:211–237

Zulauf G, Vejnar Z (1998) Zur geologischen Entwicklung des Teplá-Kristallins und des Marienbader Komplexes (Böhmische Masse). Jahresb Mit Oberrhein Geol V 80:195–221

Zulauf G, Dörr W, Fiala J,Vejnar Z (1997) Late Cadomian crustal tilting and Cambrian transtension in the Teplá-Barrandian unit (Bohemian Massif, Central European Variscides). Geol Rundsch 86:571–584

Zulauf G, Schitter F, Riegler G, Finger F, Fiala J, Vejnar Z (1999) Age constraints on the Cadomian evolution of the Teplá Barrandian unit (Bohemian Massif) through electron microprobe dating of metamorphic monazite. Z Deutsch Geol Ges 150:627–639

Zulauf G, Bues C, Dörr W, Vejnar Z (2002) 10 km minimum throw along the West Bohemian shear zone: evidence for dramatic crustal thickening and high topography in the Bohemian Massif (European Variscides). Int J Earth Sci 91:850–864